On Earth's Mantle Constitution and Structure from Joint Analysis of Geophysical and Laboratory-Based Data: An Example

Author(s):
Khan, Amir

Publication date:
2016-01

Permanent link:
https://doi.org/10.3929/ethz-b-000110574

Originally published in:
Surveys in Geophysics 37(3), https://doi.org/10.1007/s10712-015-9353-z

Surv Geophys (2016) 37:149–189
DOI 10.1007/s10712-015-9353-z

On Earth's Mantle Constitution and Structure from Joint Analysis of Geophysical and Laboratory-Based Data: An Example

Amir Khan[1]

Received: 28 October 2014 / Accepted: 25 November 2015 / Published online: 5 January 2016

Abstract Determining Earth's structure is a fundamental goal of Earth science, and geophysical methods play a prominent role in investigating Earth's interior. Geochemical, cosmochemical, and petrological analyses of terrestrial samples and meteoritic material provide equally important insights. Complementary information comes from high-pressure mineral physics and chemistry, i.e., use of sophisticated experimental techniques and numerical methods that are capable of attaining or simulating physical properties at very high pressures and temperatures, thereby allowing recovered samples from Earth's crust and mantle to be analyzed in the laboratory or simulated computationally at the conditions that prevail in Earth's mantle and core. This is particularly important given that the vast bulk of Earth's interior is geochemically unsampled. This paper describes a quantitative approach that combines data and results from mineral physics, petrological analyses of mantle minerals, and geophysical inverse calculations, in order to map geophysical data directly for mantle composition (major element chemistry and water content) and thermal state. We illustrate the methodology by inverting a set of long-period electromagnetic response functions beneath six geomagnetic stations that cover a range of geological settings for major element chemistry, water content, and thermal state of the mantle. The results indicate that interior structure and constitution of the mantle can be well-retrieved given a specific set of measurements describing (1) the conductivity of mantle minerals, (2) the partitioning behavior of water between major upper mantle and transition-zone minerals, and (3) the ability of nominally anhydrous minerals to store water in their crystal structures. Specifically, upper mantle water contents determined here bracket the ranges obtained from analyses of natural samples, whereas transition-zone water concentration is an order-of-magnitude greater than that of the upper mantle and appears to vary laterally underneath the investigated locations.

✉ Amir Khan
amir.khan@erdw.ethz.ch

[1] Institute of Geophysics, ETH Zürich, Sonneggstr. 5, 8092 Zürich, Switzerland

Keywords Mantle structure · Composition · Temperature · Water circulation · Mantle melting · Electrical conductivity · Phase equilibria · Electromagnetic sounding · Inversion

1 Introduction

As most of Earth's interior remains inaccessible from the geochemical point of view, geophysical methods based on seismic, geodetic, gravity, and electromagnetic sounding studies play prominent roles because of their ability to define structure on large scale lengths and depths based on measurements acquired from surface instrumentation. Global seismic tomography images, for example, have provided a window into Earth's interior. These models have linked velocity anomalies with tectonic features and provide information on its current physical structure (e.g., Kustowski et al. 2008; Ritsema et al. 2011; Schaeffer and Lebedev 2013). However, as physical properties such as seismic wave speeds can only provide clues about the underlying processes that are responsible for the wave-speed variations that are imaged, they are not an end in themselves. Moreover, because density is generally poorly constrained, applying the information provided by the tomographic images in a geodynamical sense is not straightforward. Given the fundamental nature of these limitations, the emphasis should be on producing physically realistic models. This, however, requires the use of physical constraints that originate in laboratory measurements of mantle minerals at the conditions relevant to Earth's interior, i.e., the compilation of mineral physics databases that will allow us to model mantle structure as a function of pressure, temperature, and composition.

With this in mind, we consider a joint formalism for retrieving information about Earth's interior from geophysical data. Rather than relying on the elastic properties of the Earth, here we focus on electrical conductivity, a complementary physical property for understanding Earth's interior. In particular, we will consider electromagnetic sounding data in combination with mineral phase equilibrium computations and laboratory measurements of electrical conductivity to infer mantle thermo-chemical state, and water content with a view to drawing implications for mantle melting. This has become possible through improved laboratory techniques that have increased understanding of the mechanisms and physico-chemical parameters governing charge transport in rocks and minerals at mantle pressure and temperature conditions (e.g., Shankland 1979; Tyburczy and Fisler 1995; Dobson and Brodholt 2000a; Nover 2005; Tyburczy 2007; Yoshino 2010; Pommier and Le Trong 2011; Karato and Wang 2013). These observations bring the possibility of using data measured at small scales (laboratory) and applying them to larger scales (local, regional, continental). Such an approach enables comparison between geophysical field and laboratory measurements and facilitates interpretation of various conductivity structures and anomalies in terms of measured parameters (e.g., Shankland 1975; Duba 1982; Dobson and Brodholt 2000b; Xu et al. 2000; Khan et al. 2006; Verhoeven et al. 2009; Yang 2011; Pommier 2014).

The purpose of the present study is therefore to describe a methodology for making quantitative inferences about Earth's mantle structure and constitution from geophysical, geochemical, and petrological data. In this sense, the present study does not represent a formal review of geophysical methods, data, analysis and interpretation techniques, but can be considered a tutorial. The goal here is to show what can be learned about the physico-chemical structure and constitution of Earth's mantle by combining geophysical data

analysis with data obtained from laboratory measurements and experimental investigations (mineral physics data) in order that fundamental parameters of interest (chemical composition and temperature) can be inverted for directly. Following the description of the methodology, data, and theoretical concepts underlying the approach, we consider a case study to highlight the advantages over more traditional approaches where inference is typically considered in a decoupled manner (field-derived estimates are compared to laboratory measurements and often only quantitatively), rather than in coupled form, i.e., integration of all relevant information.

2 Making Sound Inferences: Joint Geophysical-Thermodynamic Modeling

In determining the structure and constitution of Earth's interior, use of both geophysical and geochemical methods has proved important. However, given that the vast majority of Earth's interior is geochemically unsampled, direct measurements or numerical computations of physical properties (e.g., seismic wave-speed, density, and electrical conductivity) of natural samples and analogs at conditions of the deep Earth allow us to compare with physical properties obtained from field geophysical models. These sources constitute a large complement of information that can help constrain possible compositions, temperatures, and mineralogy of Earth's mantle and core. Traditionally, therefore, inference proceeds in the following manner

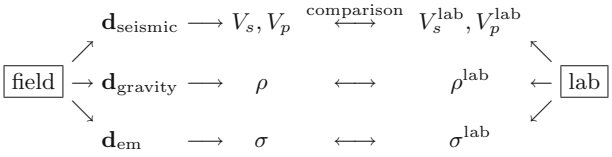

where **d** is short for field-derived data (seismic, gravimetric, geodetic, and/or electromagnetic sounding), $V_{\text{s}}, V_{\text{p}}, \rho$, and σ are geophysically estimated ("$\longrightarrow$") seismic P- and S-wave speeds, density, and electrical conductivity, respectively; "lab" is shorthand for laboratory experiments and numerical computations and the physical properties that derive from these ("$\longleftarrow$").

This type of analysis is exemplified in current conductivity-based estimates of mantle water content: from comparison of laboratory-based conductivity models with average profiles constructed from a global conductivity model (e.g., Kelbert et al. 2009), Karato (2011) determines an average transition-zone water content of ~ 0.1 wt%. However, it is our contention that the influence and trade-offs of all major parameters are too complex to justify inferences that rely on qualitative comparison of a simplified laboratory-constructed conductivity model (based on, e.g., adiabaticity, homogeneity, preliminary reference Earth model (PREM) pressure profile, and pyrolite-based mineralogy) with typically regularized geophysical profiles.

A more definitive and quantitative approach, therefore, would be to combine the different pieces, i.e., data and results from mineral physics experiments, geochemical and petrological analyses of mantle minerals, and geophysical inverse calculations, to directly transform geophysical data into the fundamental parameters of interest (mantle composition and thermal state). This means that the above inference sequence takes the following form

$$\begin{array}{ccccc} c & & V_s, V_p & \longrightarrow & \mathbf{d}_{\text{seismic}} \\ & \searrow \quad \nearrow & & & \\ & M & \rho & \longrightarrow & \mathbf{d}_{\text{gravity}} \\ & \nearrow \quad \uparrow \quad \searrow & & & \\ T & \mathbf{d}_\chi & \sigma & \longrightarrow & \mathbf{d}_{\text{em}} \end{array} \tag{1}$$

where c is an appropriately defined composition, T is temperature, M is modal mineralogy, and the remaining parameters are as above. $\mathbf{d}_\chi$ represents miscellaneous data sets (where available) that derive from e.g., petrological experiments and/or theoretical/numerical calculations. Note that insertion of $\mathbf{d}_\chi$ in the above scheme is arbitrary and depends on the nature of the data that are considered (this will be illustrated in Sect. 6 with a specific application). Arrows indicate the various methodologies employed (e.g., thermodynamic and equation-of-state modeling, geophysical response estimation) to compute geophysical data from the fundamental parameters. Should we be interested in solving the inverse problem, i.e., determining the fundamental parameters from data, we simply reverse the sense of the arrows (this will be considered in more detail in Sect. 6). Thermodynamically consistent petrological-geophysical approaches have also been advocated by Afonso and colleagues in a number of studies (e.g., Afonso et al. 2008, 2013a, b, 2015; Fullea et al. 2012, 2014; Jones et al. 2014; Kuskov et al. 2014).

Central to the method is the ability to predict geophysical response functions from models of the thermo-chemical state of Earth's mantle. To facilitate this, we rely on self-consistent thermodynamic calculations of mineral phase equilibria and their physical properties that allows for the prediction of radial profiles, e.g., electrical conductivity and density that depend only on composition, temperature, and pressure. There are several advantages to this interdisciplinary method: (1) adherence to the fundamental parameters c and T implies that widely different data sets become naturally integrated allowing for joint inversion without having to resort to unfounded or unwarranted prior assumptions regarding data dependence; (2) discontinuities associated with mineral phase transformations such as those that are observed to occur at the 410-, 520-, and 660-km seismic discontinuities are an integral part because their location and size are functions of the particular composition, temperature, and pressure considered; (3) a whole range of thermo-chemical models and parameters can be tested. Importantly, the use of different data sets (geophysical, geochemical, petrological) can serve to break the trade-off between various parameters (e.g., mantle temperature and water content). This will be specifically illustrated here with the inversion of electromagnetic sounding data and incorporation of experimental data on the mineral water partitioning behavior and water saturation levels.

Keeping in mind the above inference scheme, this tutorial commences by describing the thermodynamic method (Sect. 3), i.e., construction of the mineral assemblage, followed by an outline of the mineral physics database (Sect. 4), including electrical conductivity data and parameters, mantle water storage capacity and water partitioning, and outlines of the effects of partial melting, grain-boundary conduction, and oxygen fugacity. Next, we describe the construction of self-consistently computed bulk electrical conductivity profiles (Sect. 5). In the last section (Sect. 6), we illustrate the methodology by applying it to the estimation of mantle water content underneath a number of localities distributed across the globe and end with a short discussion of the results.

As a final remark and keeping in mind the tutorial nature of this study, we would like to emphasize that it is not the purpose here to discuss the intricacies of and problems related

to measuring mineral physics data such as electrical conductivity of mantle minerals, water partition coefficients, and mantle mineral water storage capacities. Instead, we focus on specific sets of experimental data, e.g., laboratory mineral conductivity data compiled in previous studies (Khan and Shankland 2012; Koyama et al. 2014) and updated with recent measurements where available. Although a particular choice of mineral physics data set might possibly influence the outcome, we emphasize that this is less important in the context of a tutorial. Indeed, the methodology is so generally formulated that new and/or additional data sets are easily incorporated.

3 Computation of Mantle Mineral Phase Equilibria

Mantle composition can be parameterized in terms of a single depth-dependent variable that represents the weight fraction of basalt in a basalt-harzburgite mixture (e.g., Xu et al. 2008; Khan et al. 2009; Ritsema et al. 2009; Zunino et al. 2011). For a given radially varying basalt fraction $f(r)$ mantle composition $\mathbf{X}(r)$ is computed from

$$\mathbf{X}(r) = f(r)\mathbf{X}_{\mathrm{B}} + [1 - f(r)]\mathbf{X}_{\mathrm{H}} \tag{2}$$

where $\mathbf{X}$ is composition within the CFMASN model chemical system comprising the oxides CaO-FeO-MgO-Al_2O_3-SiO_2-Na_2O, and $\mathbf{X}_{\mathrm{H}}$ and $\mathbf{X}_{\mathrm{B}}$ are CFMASN basalt and harzburgite end-member model compositions, respectively (Table 1). This chemical model accounts for $\sim 98\,\%$ of the mass of Earth's mantle (e.g., Irifune 1994).

The advantage of this compositional model (Eq. 2) is its relation to the dynamical processes that are responsible for generating and maintaining heterogeneities in the mantle. Heterogeneities are believed to be produced by a sequence of processes that initiate with asthenospheric melting at mid-ocean ridges (e.g., Ringwood 1975), followed by subduction of physically and chemically stratified oceanic lithosphere, to chemical segregation of slabs as they penetrate into the deep mantle and become entrained in the mantle flow (e.g., Tackley et al. 2005; Davies 2006) producing an increase in basalt in the mid-to-lower mantle as observed in some models (e.g., Xie and Tackley 2004; Nakagawa et al. 2009; Khan et al. 2009; for a discussion of alternative models see, e.g., Tackley 2000, 2012). These heterogeneities comprise a range of length scales from microscopic to 1000 km-sized scatterers in the mantle for which ample seismological and chemical evidence is accumulating (e.g., Hofmann 1997; Helffrich and Wood 2001; Helffrich 2002, 2006).

We employ the free-energy minimization strategy described by Connolly (2009) to predict rock mineralogy, elastic moduli, and density as a function of pressure, temperature,

Table 1 Model end-member bulk compositions in wt%

Component	Basalt ($\mathbf{X}_{\mathrm{B}}$)	Harzburgite ($\mathbf{X}_{\mathrm{H}}$)
CaO	13.05	0.5
FeO	7.68	7.83
MgO	10.49	46.36
Al_2O_3	16.08	0.65
SiO_2	50.39	43.64
Na_2O	1.87	0.01

Basalt and harzburgite compositions are taken from Khan et al. (2009)

and bulk composition. For this purpose we use the thermodynamic formulation of Stixrude and Lithgow-Bertelloni (2005) with parameters as in Stixrude and Lithgow-Bertelloni (2011). Although Gibbs energy minimization has long been advocated for geophysical problems (e.g., Sobolev and Babeyko 1994; Bina 1998; Fabrichnaya 1999), it is only in the last decade that the availability of comprehensive thermodynamic databases (e.g., Khan et al. 2006; Stixrude and Lithgow-Bertelloni 2005, 2011; Ricard et al. 2005; Piazzoni et al. 2007) have made the application of such calculations feasible for geophysical models of Earth's entire mantle.

In the equilibrium model adopted here, it is assumed that harzburgitic and basaltic components are chemically equilibrated and bulk properties are computed from the mineralogy obtained by free-energy minimization for the resulting bulk composition. Phase equilibria and corresponding bulk conductivity profiles are illustrated and discussed further in Sect. 5. In an alternative model, termed the mechanical mixture model, Xu et al. (2008) considered the extreme scenario in which pyrolitic mantle has undergone complete differentiation to basaltic and harzburgitic rocks. In this model, bulk properties are computed by averaging the properties of the minerals in the basaltic and harzburgitic end-members. From a geophysical viewpoint, however, there is no argument for the mechanical mixture model nor the equilibrium model, whereas from a petrological viewpoint, it can be said that, while the mechanical mixture model plausibly depicts the influence of chemical segregation on the equilibrium model, it cannot be said to be a more realistic end-member for the Earth's mantle because it is inconsistent with the products of mid-ocean ridge volcanism (Khan et al. 2009). Moreover, the arguments put forward by Xu et al. (2008) in favor of the mechanical mixture model are based on simplified and qualitative comparison with radial one-dimensional models of the Earth (e.g., PREM), which neglects a lot of the apparent complexity of current three-dimensional models (e.g., Khan et al. 2013).

To illustrate the thermodynamic approach, we computed phase equilibria for the two end-member compositions basalt and harzburgite (Table 1) and pyrolite (corresponding to a basalt fraction $f \sim 0.2$). The phase equilibria are shown in Fig. 1. To further illustrate the advantage of the methodology, we also show corresponding bulk conductivity profiles (to be described in the following section). The importance of considering the phase equilibrium-approach as illustrated in Fig. 1 is evident in the three bulk conductivity profiles. We clearly observe that (1) the computed bulk conductivities differ and (2) the location and size of discontinuities e.g., olivine $\rightarrow$ wadsleyite and ringwoodite $\rightarrow$ bridgemanite + ferropericlase (equivalent of the 410 and 660-km seismic discontinuities) vary considerably and depend strongly on the particular mineralogy and thus thermo-chemical setting. These variations in physical properties will have a strong influence on the computed electromagnetic response, which, as a consequence, can be used to distinguish the various profiles and by inference the thermo-chemical state of the mantle. This emphasizes the importance of constructing profiles of physical properties that are anchored in laboratory measurements.

The present thermodynamic model has limitations that might have consequences for its validity to Earth's mantle. First, the NCFMAS model system precludes consideration of redox effects that are expected to be important if native or ferric iron are present in the Earth's mantle. We neglect such effects both out of necessity, in that the thermodynamic data required to model redox are lacking, and simplicity, in that we are unaware of any work that suggests that ferrous iron is not the dominant form of iron in Earth's mantle.

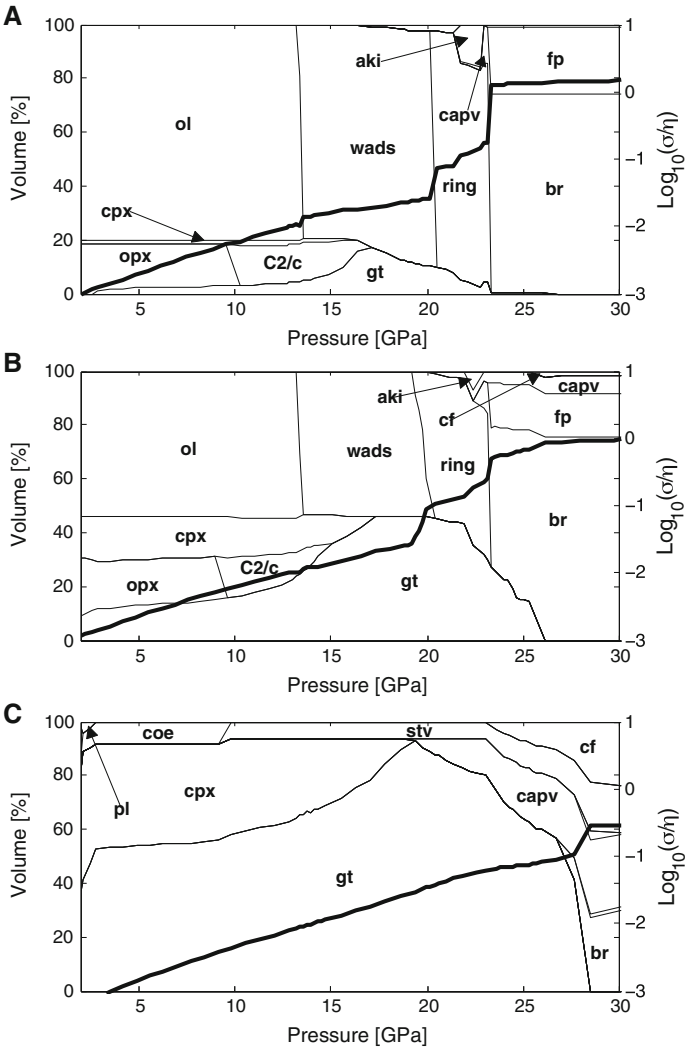

Fig. 1 Variations in phase proportions (modal mineralogy) and bulk electrical conductivity in the upper mantle, transition-zone and uppermost lower mantle (pressure range 2–30 GPa corresponding to 50–750 km depth). Electrical conductivity (*bold solid lines*) and phase equilibria are calculated for three different mantle compositions in the NCFMAS system (comprising oxides of the elements Na_2O-CaO-FeO-MgO-Al_2O_3-SiO_2): harzburgite (**a**), pyrolite (**b**), and MORB (**c**), along the mantle adiabat of Brown and Shankland (1981) (not shown). For the particular calculations performed here, we consider water contents of 0.001 wt% (ol), 0.005 wt% (opx), 0.01 wt% (stv), and 0.01 wt% (wads and ring). Phases are olivine (ol), orthopyroxene (opx), clinopyroxene (cpx), pl (plagioclase), coe (coesite), stv (stishovite). high-pressure Mg-rich cpx (C2/c), garnet (gt), wadsleyite (wad), ringwoodite (ring), akimotoite (aki), calcium silicate perovskite (ca-pv), ferropericlase (fp), bridgemanite (br; formerly perovskite), and calcium ferrite (cf). $\eta = 1$ S/m

Components and phases not considered include H_2O, TiO_2, Cr_2O_3, and partial melt because of lack of thermodynamic data. The effect of H_2O on phase equilibria will be discussed further in Sect. 5.1.1.

4 Mineral Physics Database

4.1 Electrical Conductivity

The electrical conductivity of the minerals making up Earth's crust and mantle depends on several parameters, including temperature, pressure, major element chemical composition, oxygen fugacity, and, where present, water content. In the following, we will provide a brief summary of the influence of the aforementioned parameters on mineral electrical conductivity, which have to a large extent been measured for most lower crustal, upper mantle, transition-zone, and lower mantle minerals (for recent in-depth reviews we refer the reader to, e.g., Nover 2005; Tyburczy 2007; Yoshino 2010; Yang 2011; Karato and Wang 2013; Yoshino and Katsura 2013; Pommier 2014).

As summarized by, e.g., Tyburczy and Fisler (1995), experimental results show that mechanisms of mineral conductivity depend on temperature and pressure according to an Arrhenius relation

$$\sigma = \sigma_o \exp\left[-\frac{H}{kT}\right] \tag{3}$$

where σ_o is the so-called pre-exponential factor, $H = E + PV$ is activation enthalpy, P is pressure, and E and V are activation energy and volume, respectively, T is temperature, and k is Boltzmann's constant. The parameters σ_o, E, and V depend specifically on the charge transport mechanism in operation. In relation hereto, mineral conductivity σ typically arises from several charge transport mechanisms that sum in parallel, viz.

$$\sigma = \sigma_i + \sigma_h + \sigma_p \tag{4}$$

where σ_h, σ_p, and σ_i signify conductivity arising from small polaron conduction (hopping of electrons between ferric and ferrous iron sites), migration of protons, and ionic conduction (migration of Mg-site vacancies), respectively.

Since the suggestion of Karato (1990) that the presence of water is able to increase electrical conductivity by several orders through conduction by protons, there have been numerous laboratory measurements of the conductivity of hydrous minerals. Comparison with field-derived conductivities indicate possible average water contents of ~ 0.01 wt% in the upper mantle and ~ 0.1 wt% in the transition zone (e.g., Karato 2011). Because of discrepancies between some laboratory measurements, a possibly "dry" mantle is, however, also not at variance with current field estimates (e.g., Yoshino et al. 2006, 2008a; Manthilake et al. 2009). While the issue has been debated (e.g., Karato and Dai 2009; Yoshino and Katsura 2009a, 2012a, 2013; Karato 2011; Karato and Wang 2013), it is yet to be resolved (alternative models based on existing measurements has been proposed by Jones et al. (2012) and more recently by Gardés et al. (2015)). As discussed by Khan and Shankland (2012) and Jones (2014), the difficulty for the community is that somewhat conflicting results are obtained that depend on which laboratory measurements are employed. For a discussion of quantitative differences between the various measurements, we refer the reader to a previous study (Khan and Shankland 2012) where we considered the electrical conductivity data based on the measurements of (1) Yoshino, Katsura, and

coworkers and (2) Karato, Dai, and coworkers. The discrepancies highlight the difficulty of the measurements and more than anything point to the need for a continued effort to improve or remeasure these, preferably by a third party.

For these reasons, and because no new measurements have been reported by Karato, Dai, and coworkers since the study of Khan and Shankland (2012), we restrict ourselves largely to the results of Yoshino, Katsura, and coworkers for hydrous olivine, orthopyroxene, wadsleyite and ringwoodite (e.g., Yoshino 2010; Yoshino and Katsura 2013). Relative to Khan and Shankland (2012) the conductivity database of Yoshino, Katsura, and coworkers has been updated and expanded to include recent measurements for akimotoite, hydrous orthopyroxene and stishovite, and ferropericlase (iron-dependent), in addition to a corrected value for the water-dependence of wadsleyite (Yoshino and Katsura 2012b). As discussed in detail in Khan and Shankland (2012), differences in conductivity data between the various groups is such that inverted mantle water content, for example, is model dependent. As a consequence, any inferences made based on a particular conductivity database have to be considered carefully. Because we rely on a stochastic inversion method, uncertainties in measured conductivity parameters are taken into account and we thereby automatically allow for larger variations.

Minerals of interest include olivine (ol), orthopyroxene (opx), clinopyroxene (cpx), garnet (gt), the high-pressure polymorph of cpx (C2/c), stishovite (stv), akimotoite (aki), wadsleyite (wads), ringwoodite (ring), ferropericlase (fp), perovskite (pv), calcium perovskite (ca-pv), and calcium ferrite (cf). The conductivity data for these minerals are briefly summarized below.

4.2 Conductivity Data and Parameters

The conductivity of olivine (ol) as a function of temperature, pressure, water and Fe content, and oxygen fugacity is given by (Yoshino et al. 2009, 2012b)

$$\begin{aligned}\sigma &= \sigma_o^i \exp\left[-\frac{H_i}{kT}\right] + \sigma_o^h X_{\mathrm{Fe}} \exp\left[-\frac{(E_0 - \alpha X_{\mathrm{Fe}}^{1/3}) + P(V_0 - \beta X_{\mathrm{Fe}})}{kT}\right] \\ &\quad + \sigma_o^p C_w \exp\left[-\frac{H_p^0 - \alpha_p C_w^{1/3}}{kT}\right]\end{aligned} \tag{5}$$

where X_{Fe} and C_w are Fe and water content (in wt%), respectively, α and β are geometrical factors, and it is implicitly assumed (here and in the following) that each pre-exponential term σ_o^i, σ_o^h, and σ_o^p also includes an oxygen fugacity term of the form $f_{\mathrm{O}_2}^q$, where q is a constant (see Sect. 4.4 for further discussion). The remaining parameters are as defined before (see Eqs. 3–4).

For clinopyroxene (cpx) and garnet (gt), we model conductivity using Eq. 3 with parameters determined by Xu and Shankland (1999) and Yoshino et al. (2008b), respectively. Note that, for gt, we rely on the values for low-Fe majorite garnet representative of pyrolite-type compositions. Yoshino et al. (2008b) have also measured conductivity of majorite garnet expected for MORB-type compositions, which contain more Fe, and is thus more conductive relative to what is used here. Lack of data to model these variations quantitatively precludes its use here. For hydrous orthopyroxene (opx), we employ the data and parameterization of Zhang et al. (2012)

$$\sigma = \sigma_o^h \exp\left[-\frac{H_h}{kT}\right] + \sigma_o^p C_w \exp\left[-\frac{H_p^0 - \alpha C_w^{1/3}}{kT}\right] \quad (6)$$

In the case of hydrous stishovite (stv), we rely on the measurements performed by Yoshino et al. (2014) and model conductivity according to

$$\sigma = \sigma_o^p C_w \exp\left[-\frac{H_p^0 - \alpha C_w^{1/3}}{kT}\right] \quad (7)$$

For hydrous wadsleyite (wads), we employ the model and data of Yoshino and Katsura (2012a, b) (Eq. 6), whereas in the case of hydrous, iron-bearing ringwoodite (ring), we rely on the results of Yoshino and Katsura (2009b) and Yoshino et al. (2008a, 2012b), respectively, and model ringwoodite conductivity following Eq. 4. In the case of akimotoite (aki), we employ the data and model of Katsura et al. (2007) given by Eq. 3. For lower mantle minerals bridgemanite (br; formerly perovskite) and ferropericlase (fp), we rely on the measurements of Xu et al. (1998) for Al-bearing bridgemanite and Yoshino et al. (2011) for iron-bearing ferropericlase (fp), respectively. The conductivity of Al-bearing bridgemanite is modeled after Eq. 3, while that of iron-bearing ferropericlase is modeled according to

$$\sigma = \sigma_o^h X_{\mathrm{Fe}} \exp\left[-\frac{(E_0 - \alpha X_{\mathrm{Fe}}^{1/3}) + P(V_0 - \beta X_{\mathrm{Fe}}^{1/3})}{kT}\right] \quad (8)$$

Conductivities for all minerals are summarized in Fig. 2 as a function of temperature, pressure, water, iron content, and oxygen fugacity. Minor phases for which conductivity data are lacking include the high-pressure polymorph of cpx (C2/c), calcium perovskite (ca-pv), and calcium ferrite (cf). Following previous work (Khan et al. 2006) we employ the conductivity data for opx as a proxy for C2/c, while for ca-pv conductivity is assumed equal to Al-free br, because Al is less soluble in ca-pv than in br. It was shown earlier (Khan et al. 2011) that the contribution to bulk conductivity from a phase making up <10 vol% is negligible and produces a difference of <0.02 log units. Based on this, little error is incurred by omitting the conductivity contribution of calcium ferrite (cf). Finally, DHMS phases (dense hydrous magnesium silicates) that are potentially important for transport of water to the deeper mantle through subduction are not considered here because of lack of thermodynamic data. Conductivities of these phases have been measured by Guo and Yoshino (2013).

4.3 Mantle Water Storage Capacity and Water Partitioning

Water storage capacities of mantle minerals or their assemblages have been given ample consideration in the light of water's importance in relation to mantle melting processes. Water storage capacity is defined as the maximum amount of water that a mineral is able to accommodate in its structure without precipitating a water-rich fluid or hydrous melt (e.g., Hirschmann et al. 2005, 2009; Keppler and Bolfan-Casanova 2006). This implies that at locations in the upper mantle, for example, where the water content exceeds the local storage capacity hydrous melting ensues (e.g., Litasov 2011). It has been suggested that this occurs when advected water-rich material from the transition zone crosses into the upper mantle producing melt that collects at the base of the upper mantle (e.g., Young

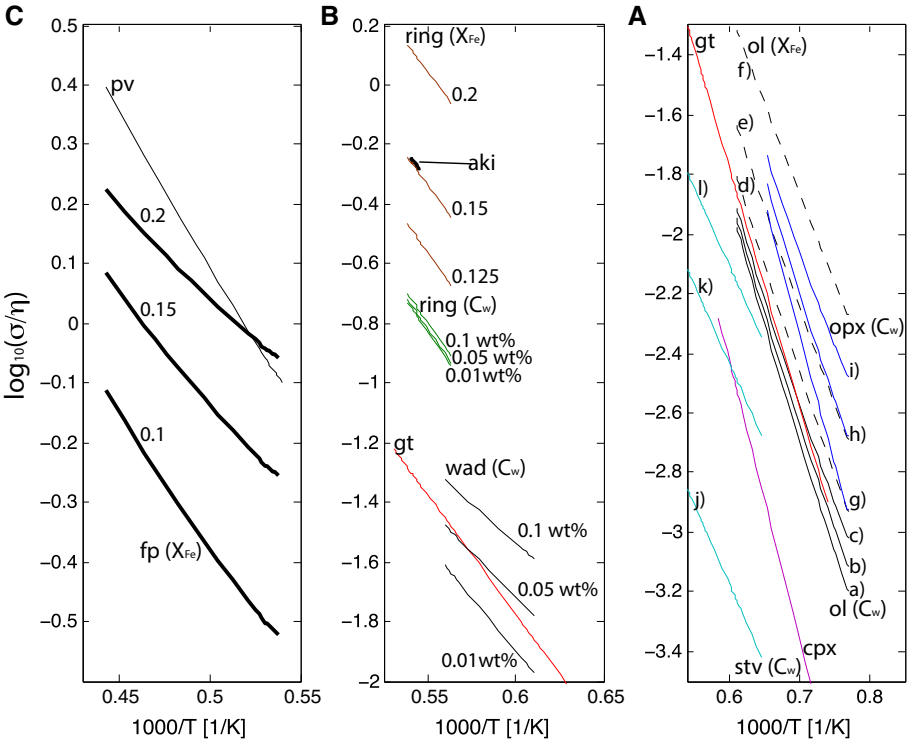

Fig. 2 Summary of major *upper mantle* (**a**), *transition zone* (**b**), and *lower mantle* (**c**) single mineral electrical conductivities based on laboratory measurements as a function of inverse temperature, water (C_w) and iron (X_{Fe}) content. Phases are: ol (olivine), opx (orthopyroxene), cpx (clinopyroxene), gt (garnet), stv (stishovite), wads (wadsleyite), ring (ringwoodite), aki (akimotoite), fp (ferropericlase), pv (perovskite/bridgemanite). In plot **a** lines *a*)–*c*) indicate the conductivity of hydrous ol for 0.001, 0.005, and 0.01 wt% H_2O, respectively (for fixed $X_{Fe} = 0.1$). Lines *d*)–*f*) show variation in conductivity of olivine as a function of iron content and correspond to X_{Fe} = 0.125, 0.15, and 0.2, respectively (for a fixed water content of 0.001 wt%). Lines *g*)–*i*) are for hydrous opx with water contents of 0.001, 0.005, and 0.01 wt% H_2O, respectively. Lines *j*)–*l*) show conductivity of hydrous stv for water contents of 0.001, 0.005, and 0.01 wt% H_2O, respectively. In plot **b** conductivity variations of hydrous ringwoodite are computed for $X_{Fe} = 0.1$, whereas the variations in conductivity of ringwoodite as a function iron content are for 0.01 wt% H_2O. Stability field of each mineral is computed based on the assumption of a fixed pyrolitic bulk composition and the mantle adiabat of Brown and Shankland (1981). To model stv conductivity we assumed a fixed basalt composition. Mantle compositions are compiled in Table 1. See main text for further discussion. $\eta = 1$ S/m

et al. 1993; Kawamoto et al. 1996; Litasov and Ohtani 2002; Bercovici and Karato 2003). The lateral extent of such a melt layer just above the transition zone is unclear and might be either global (Bercovici and Karato 2003) or local (Hirschmann 2006; Toffelmier and Tyburczy 2007; Khan and Shankland 2012). Whatever its extent, the presence of such a layer could play a strong role in determining the flux of water and other chemical elements between the various parts of the mantle (e.g., Bercovici and Karato 2003).

The nominally anhydrous minerals making up mantle peridotite incorporate water as hydrogen defects in their structures (e.g., Bell and Rossmann 1992; Kohlstedt et al. 1996; Bolfan-Casanova et al. 2000). Hydrogen solubility in nominally anhydrous silicates controls melting in water-containing systems (dependent on P, T, and f_{O_2}) and occurs when

silicates become supersaturated with H_2O. Note that water is not the only volatile capable of producing melting in the mantle. Melting associated with CO_2-containing systems and, more generally, mantle in the presence of a C–O–H fluid, is also believed to be important (e.g., Dasgupta and Hirschmann 2010; Litasov 2011), but beyond the scope of the present study.

The amount of water that the nominally anhydrous upper mantle minerals (e.g., olivine, clinopyroxene, orthopyroxene, and garnet) can hold has been determined in high-temperature and high-pressure petrology experiments of which a large part has concentrated on the volumetrically dominant mineral olivine (e.g., Kohlstedt et al. 1996; Mosenfelder et al. 2006; Smyth and Jacobsen 2006; Litasov et al. 2007; Férot and Bolfan-Casanova 2012). Measurements on natural samples, for example, have shown that olivine, the most abundant mineral in the upper mantle, contains far less water than pyroxenes, the next-most abundant minerals (e.g., Peslier et al. 2010; Peslier and Bizmis 2015). In spite of this observation, the water content of the upper mantle is still believed to be largely controlled by olivine due to a marked increase in its solubility with pressure and water fugacity as observed experimentally (e.g., Kohlstedt et al. 1996; Mosenfelder et al. 2006; Smyth and Jacobsen 2006). This contrasts with observations of pyroxenes, where hydrogen is coupled to aluminum content which decreases with increasing pressure, in particular after the onset of the garnet stability field (e.g., Rauch and Keppler 2002; Aubaud et al. 2004; Hauri et al. 2006; Mierdel et al. 2007; Withers and Hirschmann 2007; Ardia et al. 2012; Férot and Bolfan-Casanova 2012; Tenner et al. 2012; Novella et al. 2014; Sakurai et al. 2014). The water solubility in garnet has also been measured (e.g., Withers et al. 1998; Lu and Keppler 1997; Aubaud et al. 2004; Tenner et al. 2009; Mookherjee and Karato 2010; Novella et al. 2014), but is of lesser importance given its relatively minor abundance in the upper mantle ($\sim$10–15 % by volume for a typical pyrolitic mantle, cf. Fig. 1).

In spite of discrepancies between the various studies that mostly relate to differing experimental techniques and set-ups, these experiments show that the water solubility in olivine and garnet increases toward the bottom of the mantle from initially $\sim$0.005 to 0.015–0.02 wt% at 400 km depth, whereas for orthopyroxene and clinopyroxene water content decreases from $\sim$0.03–0.04 to 0.01–0.025 wt%. Most of these experiments were carried out on minerals from natural samples that emanate from no more than 200–250 km depth and thus suffer from having to be extrapolated to higher pressures. In summary, and as reported elsewhere (e.g., Férot and Bolfan-Casanova 2012; update, 2014), the experimental results suggest that the water storage capacity of the upper mantle is dominated by the storage capacity of olivine. Thus, to determine the storage capacity of the mantle from measurements performed on olivine the partitioning behavior of water between olivine and orthopyroxene/clinopyroxene/garnet is needed.

For the experiments above, water partition coefficients can be calculated between the various mineral phases that coexist. As we currently limit ourselves to modeling the effect of water on the conductivity of olivine and orthopyroxene in the upper mantle, we only consider the water partition coefficient between orthopyroxene and olivine (Table 2). The results summarized in this table are not exhaustive and show significant scatter, which attests to the difficulty in making these measurements. The most recent re-evaluation of the experimental results conducted by Ferot and Bolfan-Casanova is shown in Fig. 3, and includes earlier water storage capacity measurements on olivine and pyroxene, in addition to the partition coefficients between olivine and garnet and between clino- and orthopyroxene by obtained Novella et al. (2014). The storage capacity of the upper mantle is $<$0.1 wt% H_2O below the crust and increases with pressure to 0.1–0.15 wt% H_2O just above the transition zone at 400 km depth. The major current uncertainty with the

Table 2 Summary of upper mantle mineral water partition coefficients between orthopyroxene and olivine ($D_{H_2O}^{opx/ol}$). Variations in Al_2O_3 content and temperature between the different experiments are not accounted for here

Source	$D_{H_2O}^{opx/ol}$
Novella et al. (2014) at 3 GPa	~9
Novella et al. (2014) at 6 GPa	1.8
Ardia et al. (2012) at 3 GPa	~13
Ardia et al. (2012) at 6 GPa	~4.5
Férot and Bolfan-Casanova (2012, update 2014) at 3 GPa	2.2
Férot and Bolfan-Casanova (2012, update 2014) at 6 GPa	1.6
Sakurai et al. (2014) at 3 GPa	15–20
Peslier (2010)	~10

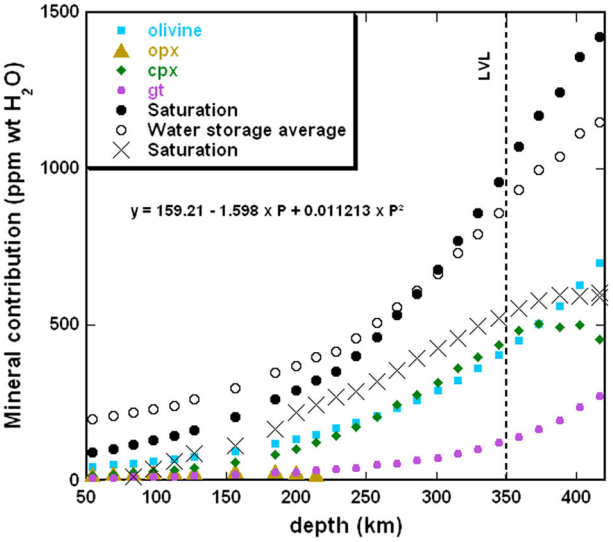

Fig. 3 Upper mantle and single mineral water storage capacity as a function of depth. *Open circles* denote the storage capacity curve of the *upper mantle* deduced by Férot and Bolfan-Casanova (2012) using a set of new FTIR extinction coefficients for olivine. *Filled circles* are based on the re-evaluation of Férot and Bolfan-Casanova (2012; update, 2014) using the latest partition coefficients deduced by Novella et al. (2014) between clinopyroxene/orthopyroxene and between garnet/olivine. See main text for details. If, instead, the high-temperature partition data of Ardia et al. (2012) are employed, a different saturation (the point where free fluid is released and produces melting) *curve* is obtained (*crosses*)

saturation curve in Fig. 3 is related to the storage capacity of Ca-rich clinopyroxene (pers. comm., N. Bolfan-Casanova 2014). For present purposes, we assume the storage capacity at the bottom of the upper mantle to be 0.15 wt% H_2O. For completeness we should note that Tenner et al. (2012) estimate the water storage capacity of peridotite at 400 km depth to be much lower 0.02–0.06 wt%. However, it should be kept in mind that storage capacity generally varies as a function of bulk composition and oxygen fugacity.

For completeness, we note that direct measurements made on xenoliths (e.g., Peslier 2010; Peslier et al. 2010) do not appear to follow the partitioning behavior between olivine and pyroxenes alluded to above (see also Peslier and Bizmis 2015). From a practical point

of view, there is much to be gained by using water partition coefficients, because of the reduction in the number of free parameters (assuming the partition coefficients known) to be determined in the inversion. However, for the purposes of this tutorial, we rely on the measurements of Férot and Bolfan-Casanova and emphasize that the results have to be viewed in the light of the particular choice of water partition coefficients. Finally, we also consider the case of no partitioning, i.e., separate determination of ol and opx water content. This will be described in Sect. 6.4.3.

The water storage capacity of the transition zone has long been known to be much larger than that of the upper mantle. This is based on the observation that the water solubility of the major transition-zone mineral wadsleyite is very high and capable of dissolving more than 3 wt% H_2O (e.g., Smyth 1987; Inoue et al. 1995; Chen et al. 2002; Bolfan-Casanova 2005; Demouchy et al. 2005; Bolfan-Casanova et al. 2006; Inoue et al. 2010). This estimate, however, was obtained at relatively low temperatures ($\sim 1200°C$) in comparison to what is expected in the transition zone ($\sim 1400-1600\,°C$) and accordingly only represents an experimentally permissible upper bound. Also, it has been observed that the water solubility of wadsleyite decreases markedly as temperature increases (e.g., Litasov and Ohtani 2003; Demouchy et al. 2005; Litasov et al. 2011). Litasov et al. (2011), for example, found that at conditions in the transition zone (13–20 GPa and 1500−1600°C), wadsleyite only contained in the range 0.37–0.55 wt% H_2O. While these results significantly decrease the maximum amount of water that can possibly be stored in the upper part of the transition zone, it nonetheless implies an increase in storage capacity of the upper mantle (between 3 and 6 times) in agreement with the results of Inoue et al. (2010). The associated water partition coefficient determined by Litasov et al. (2011) between olivine (forsterite) and wadsleyite showed a complex behavior with temperature that we do not model because of lack of systematic data. It should also be noted that the storage capacity of Fe-bearing wadsleyite is higher than that of Fe-free wadsleyite and may accommodate as much as 1 wt% H_2O at ~ 13 GPa and 1500 °C (e.g., Chen et al. 2002; Hirschmann et al. 2005, 2009).

The water storage capacity of the lower part of the transition zone, which is dominated by the mineral ringwoodite, has, based on the recent water partitioning experiments between wadsleyite and ringwoodite (Inoue et al. 2010), been determined to be around 0.15–0.3 wt% H_2O, implying a partition coefficient $D_{H_2O}^{wads/ring} \sim 2$. In the absence of measurements of the storage capacity of majorite garnet, we assume the storage capacity of the transition zone to be governed by that of wadsleyite and ringwoodite. This implies that at locations where material is advected from the transition zone into the bottom of the upper mantle and contains water in excess of the storage capacity of the upper mantle (here 0.15 wt% H_2O) hydrous melting ensues and result in layers or pockets of melt that pond on top of the 410-km seismic discontinuity.

4.4 Oxygen Fugacity

As briefly mentioned previously, electrical conductivity of mantle minerals also depends on oxygen fugacity (f_{O_2}) and through it on oxidation state that controls the number of charge carriers, e.g., electrons from ionization of Fe^{2+} to Fe^{3+}. For example, it has been observed experimentally that electrical conductivity of olivine increases as $f_{O_2}^{1/6}$ or $f_{O_2}^{2/5}$ (e.g., Schock et al. 1989; Duba and Constable 1993; Frane et al. 2005) due to an increase in ferric iron content. Although poorly quantified, there is additional experimental evidence that the conductivity of other Fe-bearing mantle phases (olivine, pyroxene, garnet,

ringwoodite, and ferropericlase) increases with increasing total iron content at the same oxygen buffer (e.g., Seifert et al. 1982; Romano et al. 2006; Omura et al. 1989; Yoshino et al. 2011, 2012b).

Oxidation state is relatively well-constrained for the upper mantle where natural samples are available (e.g., Frost and McCammon 2008). As summarized by e.g., Frost and McCammon (2008) and McCammon (2005) and based on oxygen geobarometer data, f_{O_2} in the shallow part of the upper mantle is relatively high and generally considered to be close to the QFM (Quartz-Fayalite-Magnetite) buffer. Based on thermodynamic calculations and experimental observations of natural samples, oxygen fugacity is believed to steadily decrease toward the transition zone attaining f_{O_2} values close to the IW (Iron-Wüstite) buffer (4–5 log units below QFM) leading to the likely stabilization of (Fe,Ni)-metal (e.g., O'Neill et al. 1993; Ballhaus 1995; Frost et al. 2004; Rohrbach et al. 2007). The ability of major transition-zone minerals majorite-garnet, wadsleyite, and ringwoodite to incorporate Fe^{3+} suggests that conditions in the transition zone are close to those of the deep upper mantle, i.e., quite reduced with an f_{O_2} just below the IW buffer, while f_{O_2} in the lower mantle can be calculated as lying approximately 1–2 log units below IW (e.g., Frost and McCammon 2008).

Excepting the measurements by Katsura et al. (2007) for akimotoite, all conductivity experiments discussed in Sect. 4.1 were carried out at oxygen fugacities close to or around the Mo-MoO_2 buffer, which is expected to be close to the IW buffer (e.g., O'Neill et al. 1993; Xu et al. 1998). Given that most of the mantle to which measurements are sensitive (depths > 200 km) is at an $f_{O_2} \sim$ IW, the measured conductivity parameters can be applied essentially without correction (i.e., we implicitly assume that oxygen fugacity in and beneath the upper mantle is near to that of the Mo-MoO_2 buffer).

In relation to oxygen fugacity, there has been some discussion in the literature (e.g., Huang et al. 2005; Karato 2011; Karato and Wang 2013) of the importance of correcting conductivity for f_{O_2} in spite of the fact that these are not likely to exceed 0.5-log units and therefore *a priori* not geophysically discernible (see also Jones et al. 2009). Karato (2011), for example, assumes an f_{O_2}-correction term to conductivity of the form

$$\sigma = \left(\frac{f_{O_2}}{f_{O_2}^{\mathrm{ref}}}\right)^{q} \sigma' \tag{9}$$

where f_{O_2} is oxygen fugacity, $f_{O_2}^{\mathrm{ref}}$ is a reference f_{O_2}, q is an exponent, typically small (<1), that determines f_{O_2} dependence (e.g., 1/6 for olivine), and σ' and σ are conductivity prior to and after correction, respectively.

This model was applied to the conductivity measurements of transition-zone minerals by Huang et al. (2005) that were conducted at relatively reducing conditions (Ni-NiO_2 buffer), but has been questioned by Hirschmann (2006). To quantitatively test the model of Karato (2011), Khan et al. (2014) conducted inversions with and without the correction term (Eq. 9). The inversions showed, however, that the f_{O_2}-correction term introduced made essentially no difference when compared to inversions without the term applied. The reason for this is that the f_{O_2}-correction term is not invoked self-consistently so as to model concomitant f_{O_2}-related changes to phase equilibria.

5 Constructing Laboratory-Based Electrical Conductivity Profiles

To construct aggregate mantle conductivity profiles from single mineral conductivities (Fig. 2), the conductivities need to be volumetrically averaged with the fraction of each mineral present. The need for averages arises because in general the distribution of mineral phases within the bulk rock is not known. Several averaging schemes are available for this purpose and in the following we briefly discuss some of these (for more detailed discussion the reader is referred to, e.g., Berryman 1995).

To compute conductivity bounds for multiphase materials, we employ Voigt and Reuss averages, and Hashin-Shtrikman bounds. Voigt and Reuss averages present the extreme bounds on bulk conductivity and bracket the permissible range within which the effective conductivity of the multiphase system must be contained (e.g., Waff 1974). Hashin-Shtrikman bounds are the narrowest bounds for a multiphase system in the absence of knowledge of the geometrical arrangement of the constituent phases (e.g., Hashin and Shtrikman 1962; Watt et al. 1976; Berryman 1995).

Voigt (arithmetic mean, A) and Reuss (harmonic mean, H) averages are calculated from

$$\sigma_A = \sum_i^N x_i \sigma_i \tag{10}$$

$$\sigma_H = \left[\sum_i^N \frac{x_i}{\sigma_i} \right]^{-1} \tag{11}$$

where σ_i and x_i are conductivity and volume fraction of mineral phase i, respectively, and N is the total number of mineral phases present. Note that both x_i and σ_i are functions of composition, pressure, and temperature. From the Reuss and Voigt averages, the Voigt-Reuss-Hill average (VRH) can be obtained as the arithmetic mean of the two (Hill 1963; Watt et al. 1976). The VRH average is biased toward the Voight bound (Shankland and Duba 1990). Hashin-Shtrikman bounds are determined from

$$\sigma_{\mathrm{HS}} \pm = \left[\sum_{i=1}^N \frac{x_i}{\sigma_i + 2\sigma_\pm} \right]^{-1} - 2\sigma_\pm \tag{12}$$

where $\sigma_\pm$ corresponds to minimum and maximum conductivity of the N mineral phases present. The lower bound (HS−) assumes non-interconnected conductive inclusions within a resistive matrix, and the upper bound (HS+) assumes non-interconnected resistive inclusions in a conductive matrix.

In addition to bounds, we also compute estimators using the geometric mean, the VRH average, and the effective medium theory for conducting composites. The geometric mean (GM) has the advantage of being readily computable (e.g., Shankland and Duba 1990)

$$\sigma_{\mathrm{GM}} = \prod_i \sigma_i^{x_i}. \tag{13}$$

Although not utilized here, Ji et al. (2004, see also Jones et al. 2009) advocate using a variant of the geometrical mean by employing the Voigt and Reuss averages. The effective medium theory of Landauer (1952) and generalized by Berryman (1995), on the other hand, produces a self-consistent solution (SC) that is found through iteration to satisfy (while being bounded by HS− and HS+)

$$\sum_{i=1}^{N} x_i \left[\frac{\sigma_i - \sigma_{SC}}{\sigma_i + 2\sigma_{SC}} \right] = 0 \tag{14}$$

The various conductivity bounds and estimators computed using Eqs. 10–14 are illustrated in Fig. 4. These are computed for the case of a homogeneous mantle composition with basalt fraction $f = 0$ along the mantle adiabat of Brown and Shankland (1981). In line with previous studies (e.g., Shankland and Duba 1990; Xu et al. 2000; Khan and Shankland 2012), we observe that the only estimator that consistently lies within the Hashin-Shtrikman bounds is the EMT-based solution σ_{SC}. Both VRH and GM are found to lie outside the Hashin-Shtrikman bounds for different depth ranges (this is illustrated in Fig. 4b for VRH, which appears below HS−). This, combined with Hashin-Shtrikman bounds being the narrowest possible restrictions that exist on an arbitrary isotropic multi-phase system, prompts us to consider self-consistently determined conductivity values as the most appropriate average bulk rock conductivity.

The procedure advocated here for constructing bulk conductivity profiles is advantageous over standard approaches where laboratory conductivity data on single minerals are

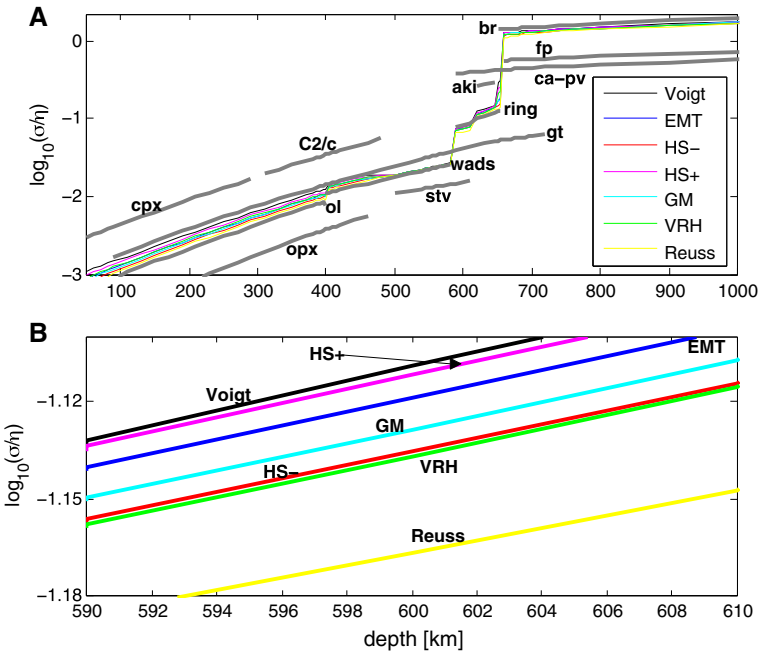

Fig. 4 Aggregate mantle conductivity profiles computed using different averaging schemes (as outlined in the main text). **a** Shows single mineral conductivities and bulk mantle conductivity profiles for the upper 1000 km and **b** shows a zoom-in on the lower part of the transition zone. Single mineral and aggregate conductivity profiles are computed on the basis of an adiabatic and homogeneous mantle (see main text for more details), which dictates the stability fields of the various minerals in **a**. The following averages and bounds are shown: arithmetic mean (Voigt); harmonic mean (Reuss); lower Hashin-Shtrikman bound (HS−); upper Hashin-Shtrikman bound (HS+); effective medium theory (EMT); Voigt-Reuss-Hill average (VRH); and geometric mean (GM). For the particular calculations performed here we consider water contents of 0.001 wt% (ol), 0.005 wt% (opx), 0.01 wt% (stv), and 0.01 wt% (wads and ring). Colour coding is the same in both plots. $\eta = 1$ S/m

typically compared, on a purely qualitative basis, to geophysically derived conductivity profiles. First, disregarding the contribution of other minerals likely results in a biased interpretation in terms of the amount of, e.g., water that is needed for a given mineral to "fit" a particular field-derived conductivity value or profile. This is apparent in Fig. 4, which shows that in attempting to "fit" a certain conductivity value at, e.g., 300 km depth in the upper mantle based on either of the minerals olivine, orthopyroxene, clinopyroxene, and garnet, the amount of water required, for example, will vary considerably depending on the particular mineral considered. Second, prominent discontinuities are generally absent in field-derived profiles due to the insensitivity of electromagnetic sounding data to sharp jumps in conductivity (e.g., Olsen 1999; Kuvshinov and Olsen 2006; Velimský 2010). Constructing conductivity profiles, therefore, that are based on laboratory measurements of mantle mineral conductivities and phase equilibria will include discontinuities at the location where the phase transformations are experimentally observed to occur (e.g., Xu et al. 2000; Khan et al. 2006, 2011; Khan and Shankland 2012; Verhoeven et al. 2009; Fullea et al. 2011). Third, quantitative comparison with data, i.e., inversion, over qualitative comparison with profiles should be emphasized. This arises because regularization methods employed in producing profiles from electromagnetic data typically results in structural features that are either unresolved or even artificial. Interpretation of such features is evidently problematic.

5.1 Miscellaneous Effects

5.1.1 Mantle Phase Equilibria in the Presence of Water

A caveat with the previous calculations is the neglect of the effect of water on mineral phase equilibria. Because relevant thermodynamic data are scarce, however, it is difficult to quantify the error produced by this omission. Theoretical and experimental studies of phase relationships in several water-containing systems including peridotite-H_2O, Mg_2SiO_4-H_2O, and $(Mg,Fe)_2SiO_4$-H_2O nonetheless permit some insight into the role of water. Figure 5 (adopted from Litasov (2011)) summarizes available experimental data on solidi and phase relationships in the peridotite-water system. Figure 5 shows that water stabilizes wadsleyite over olivine promoting upward migration of the "410-km" discontinuity, which is ultimately due to the differing water solubility of the minerals (e.g., Wood 1995; Chen et al. 2002; Smyth and Frost 2002; Frost 2003; Frost and Dolejs 2007; Litasov and Ohtani 2003, 2007; Litasov et al. 2006; Deon et al. 2011). The "660-km" discontinuity (ringwoodite → bridgemanite + ferropericlase) is also observed experimentally to move to higher pressures, i.e., deeper (e.g., Frost 2003; Litasov et al. 2006; Ghosh et al. 2013).

In comparison, given the modest change in conductivity across the olivine → wadsleyite transition seen here (Fig. 1), neglect of water on the location of the "410" appears to be a relatively minor issue. Judging from Fig. 1 depression of the "660" is likely to produce a more pronounced effect on the inductive response functions. We tested this by considering the model shown in Fig. 1b as "baseline" and depressed the "660" by 40 km (see inset in Fig. 6). According to Ghosh et al. (2013), this is equivalent to the effect induced by the presence of ~ 0.1 wt% water in the lower part of the transition zone. The test showed (Fig. 6) that the inductive response changed little as a result, indicating that water-induced changes in the "660" are at the limit of detectability with the electromagnetic response functions considered here. The response functions will be described in more detail in Sect. 6.

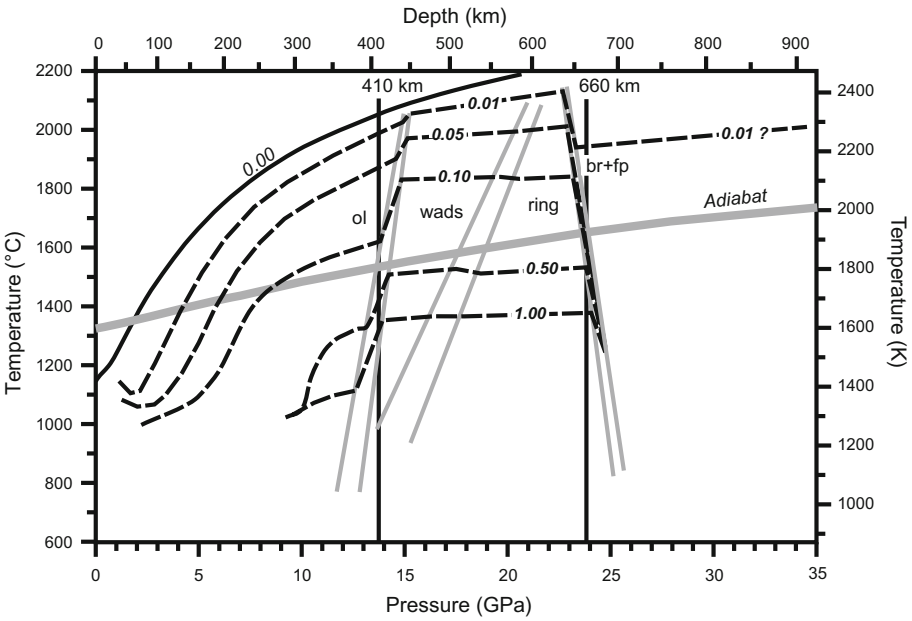

Fig. 5 Phase relationships and solidi in the H_2O-peridotite system as a function of water content. *Thin gray lines* indicate phase boundaries between major upper, transition zone, and lower mantle minerals olivine (ol), wadsleyite (wads), ringwoodite (ring), bridgemanite (br), and ferropericlase (fp), respectively. *Thick gray line* shows a mantle adiabat with a potential temperature of 1315 °C, while *black dashed lines* show the solidi of the system for various water contents (from 0 to 1 wt% H_2O). Modified from Litasov (2011)

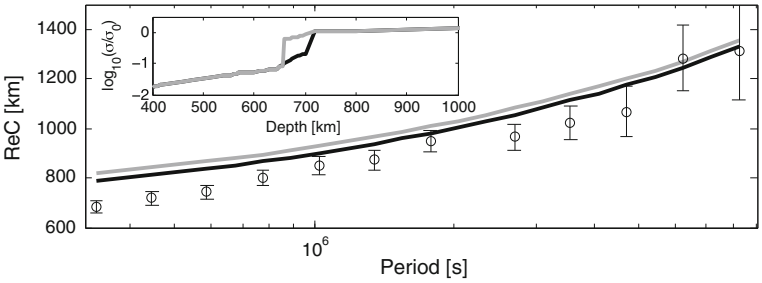

Fig. 6 Depression of the "660-km" discontinuity and corresponding changes in electromagnetic response functions (C-responses). The *inset* shows bulk conductivity profiles for which C-responses are computed with *gray* and *black lines* corresponding to discontinuities placed at 660 and 700 km depth, respectively. For comparison, observed C-responses and uncertainties (*circles* and *error bars*) for the station TUC (Tucson) are also shown

In addition to changes in phase equilibria, there is the effect on solidus temperatures in water-containing systems. The solidus decreases with increasing water content (Fig. 5). For peridotite containing 0.1 wt% water, for example, the solidus temperature at the "410-km" discontinuity can drop by 200−250°C with pressure (e.g., Aubaud et al. 2004; Hirschmann 2010; Litasov 2011). As discussed earlier, this can potentially lead to melting of material that crosses the "410-km" discontinuity as it is being advected by the background mantle flow.

5.1.2 Partial Melting

In the lower crust and upper mantle numerous zones of anomalously high electrical conductivity associated with subduction zones and other tectonic regions have been detected geophysically, particularly by magnetotelluric methods (e.g., Evans et al. 2005; Baba et al. 2006, 2010; Wannamaker et al. 2009; Worzewski et al. 2011; Becken and Ritter 2012). The conductivity associated with these regions is around 0.1 S/m or more and in active tectonic regions can be interpreted as a result of partial melting (e.g., Shankland and Waff 1977; Shankland et al. 1981; Shankland and Ander 1983) because it is difficult to explain such high conductivities in terms of an olivine-dominated upper mantle. Even in the case of a hydrated upper mantle containing as much as 0.01 wt% H_2O the conductivity is not much greater than 0.01 S/m (Khan and Shankland 2012). However, uncertainties in proton conduction model, effects of oxygen fugacity, water content, grain-boundary conduction, and variations in major element content, particularly Fe content, could potentially increase conductivity.

Presence of water in the mantle will lower the solidus (e.g., Hirth and Kohlstedt 1996; Hirschmann 2006), i.e., onset of melting will occur at a lower temperature relative to a dry mantle. Because melts are highly conductive they are often invoked as a means of explaining conductivity anomalies in the lower crust, asthenosphere, and bottom of the upper mantle (e.g., Shankland and Waff 1977; Park and Ducea 2003; Toffelmier and Tyburczy 2007; Khan and Shankland 2012; Koyama et al. 2006, 2014). Laboratory conductivity measurements of silicate melts have been conducted and found to depend strongly on chemical composition, notably sodium and water content, melt volume fraction, and melt geometry (e.g., Tyburczy and Waff 1983; Roberts and Tyburczy 1999; Partzsch et al. 2000; Gaillard 2004; ten Grotenhuis et al. 2005; Maumus et al. 2005; Pommier et al. 2010; Ni et al. 2011).

Based on recent experimental studies of the peridotite-CO_2 and eclogite-CO_2 systems or more generally peridotite and eclogite in the presence of a C–O–H fluid (e.g., Williams and Hemley 2001; Poli and Schmidt 2002; Dasgupta and Hirschmann 2010; Litasov and Ohtani 2009; Litasov 2011), Gaillard et al. (2008) suggested that the presence of very small amounts of highly conductive carbonatite melt would be sufficient to explain the observed conductive field anomalies. The initial measurements by Gaillard et al. (2008), conducted at atmospheric pressure, were subsequently redone by Yoshino et al. (2010, 2012a) at upper mantle pressures (3 GPa). Conductivity of carbonate melt-bearing olivine aggregates was found to be an order-of-magnitude higher than silicate melt-bearing olivine aggregates for the same melt fraction. Similar results were also found by Ni et al. (2011) for hydrous basaltic melt.

One way to use these results is to estimate the melt fraction that would be needed to attain a given field-derived conductivity estimate. Following this, Shankland and Waff (1977), for example, concluded that a melt fraction of a few percent is required to satisfy some high conductivity anomalies in and around the asthenosphere. This amount of melt (~ 1 %), however, is only expected around mid-ocean ridges, while away from these no more than 0.1 % is thought to be present (e.g., Hirschmann 2010). Because the combined effect on conductivity of all of the above contributions is convoluted and difficult to disentangle from knowledge of bulk conductivity only, and because we currently lack a thermodynamic model for describing the composition of hydrous silicate melts in detail, we treat melt conductivity using a simplified model based on a physical parameterization. This will be described in Sect. 6 in more detail.

5.1.3 Grain-Boundary Conduction

In addition to grain-interior conduction (described in Sect. 4.1), grain-boundary conduction has also been proposed as a potential source for increased conductivity in various regions of the upper mantle (e.g., Shankland et al. 1981; Duba and Shankland 1982; Roberts and Tyburczy 1993; Ducea and Park 2000; Yoshino et al. 2010; Poe et al. 2010). Particularly grain boundaries in the upper mantle shear zone are expected to be 1.5–2 orders of magnitude more conductive than less deformed regions in the lithosphere. Experimental observations show that grain-boundary conductivity may influence electrical conductivity measurements through the contribution of surface conduction to total rock conductivity. This occurs if transport of charge carriers along grain boundaries is faster than through the crystal lattice. Alternatively, conductivity could be reduced if grain boundaries block transport of charge carriers (e.g., Roberts and Tyburczy 1993).

Experimental evidence for the effects related to grain-boundary composition and phase is scarce (e.g., Watson et al. 2010) and in the absence of observations that support substantial systematic variations in conductivity (e.g., Duba and Shankland 1982; Roberts and Tyburczy 1993; Ducea and Park 2000; ten Grotenhuis et al. 2004; Dai et al. 2008; Watson et al. 2010; Yang and Heidelbach 2012), no corrections for grain-boundary effects are made here.

6 Geophysical Application

With a procedure for computing conductivity structure from knowledge of mantle composition and thermal state, we can invert this process to obtain information on the fundamental parameters of interest. Here, we illustrate the joint geophysical-thermodynamic methodology by inverting long-period electromagnetic sounding data to retrieve information on mantle composition, temperature, and water content.

The relationship between model $\mathbf{m}$ and data $\mathbf{d}$ is usually written as

$$\mathbf{d} = \mathrm{g}(\mathbf{m}) \tag{15}$$

where g is a generally nonlinear operator that maps from model to data space (forward problem). With reference to the inference scheme (Eq. 1) and setting $\mathbf{d}_\chi = \{\mathbf{d}_{\text{petro}}, \mathbf{d}_\sigma\}$, the forward problem comprises the following sequence

$$\begin{array}{ccccccc} & & \mathbf{d}_{\text{petro}} & & \mathbf{d}_\sigma & & \\ & & \downarrow & & \downarrow & & \\ \{f(r), T(r), \mathrm{C_w}\} & \overset{\mathrm{g_1}}{\rightarrow} & M(r) & \overset{\mathrm{g_2}}{\longrightarrow} & \sigma(r) & \overset{\mathrm{g_3}}{\longrightarrow} & \mathbf{d}_{\text{em}} \end{array} \tag{16}$$

where f, T, and C_w are the fundamental parameters (basalt fraction, temperature, and water content) that we wish to invert for, M is equilibrium modal mineralogy, σ is bulk conductivity, r is radius, $\mathbf{d}_{\text{petro}}$ are petrological data from experimental determinations of mineral water partition coefficients and storage capacity (Sect. 4.3), $\mathbf{d}_\sigma$ laboratory conductivity data (Sect. 4.2), and $\mathbf{d}_{\text{em}}$ are geophysical data in the form of C-response functions (Sect. 6.1). M and σ are secondary parameters and act as intermediaries in proceeding from fundamental parameters to computation of data. g is shorthand notation for the physical laws used in modeling data from model parameters: Gibbs free-energy minimization (g_1), construction of a bulk laboratory-based conductivity profile (g_2), and prediction of C-responses (g_3).

We employ the probabilistic approach of Tarantola and Valette (1982) to solve the nonlinear inverse problem. A detailed treatment in the context of the thermodynamic approach is given by, e.g., Khan et al. (2007), Verhoeven et al. (2009), and Afonso et al. (2013a, b). Within a Bayesian framework, the solution to the general inverse problem (Eq. 15), is given by (Tarantola and Valette 1982)

$$\Omega(\mathbf{m}) = k\mathcal{H}(\mathbf{m})\mathcal{L}(\mathbf{m}), \tag{17}$$

where k is a normalization constant, $\mathcal{H}(\mathbf{m})$ is the prior probability distribution on model parameters, i.e. information about model parameters obtained independently of the data, $\mathcal{L}(\mathbf{m})$ is the likelihood function, which can be interpreted as a measure of misfit between the observations and the predictions from model $\mathbf{m}$, and $\Omega(\mathbf{m})$ is the posterior model parameter distribution containing the solution to the inverse problem. The particular form of $\mathcal{L}(\mathbf{m})$ is determined by the observations, their uncertainties and how these can model data noise (described below).

We use the Metropolis–Hastings algorithm to sample the posterior distribution Eq. 17 in the model space (Metropolis et al. 1953; Hastings 1970). Although this algorithm is based on random sampling of the model space, only models that result in a good data fit and are consistent with prior information are frequently sampled (importance sampling). The Metropolis algorithm is capable of sampling the model space with a sampling density proportional to the target posterior probability density without excessively sampling low-probability areas. This is particularly important when we consider high-dimensional model spaces in which a large proportion of the volume may have near-zero probability density (e.g., Mosegaard and Tarantola 1995).

The main purpose for using a probabilistic inference approach to solving nonlinear inverse problems is to present the information gathered from a whole series of sampled models, rather than a single realization from the posterior distribution. To quantitatively summarize information from such a complex probability density function (PDF), standard resolution measures involving means and covariances are inadequate, and we resort to a more general approach where the statistical features of the models are of main interest.

6.1 Electromagnetic Sounding Data

Input geophysical data are electromagnetic response functions in the form of C-responses. As shown by Banks (1969), C-responses are obtained from magnetic measurements at a particular geomagnetic observatory from

$$C(\omega) = -\frac{a\tan\vartheta}{2}\frac{Z(\omega)}{H(\omega)}, \tag{18}$$

where a is mean radius of the Earth (6371.2 km), ϑ geomagnetic co-latitude, $Z(\omega)$ and $H(\omega)$ vertical and horizontal components (in the direction of geomagnetic north) of the geomagnetic field, respectively, at frequency ω. This technique is commonly referred to as the Z:H method (e.g., Olsen 1998). An inherent assumption in the Z:H method is the structure of the source field potential. Irregular variations caused by large-scale magnetospheric sources are assumed proportional to the first zonal harmonic, P_1^0, in the geomagnetic coordinate system.

To ensure that only high-quality data are inverted, C-responses were constructed using the following interdependent criteria: (1) regional C-responses are required to show quasi-1D behavior; (2) only C-responses from mid-latitude observatories were considered to

minimize influence from auroral (both poles) and equatorial source effects; (3) *C*-responses should vary smoothly and be characterized by low uncertainty and high coherency; (4) *C*-responses should cover the largest possible period range to enable sounding of the transition-zone and uppermost lower mantle. Details on data selection and processing are given in Khan et al. (2011).

Data (hourly mean values) from six geomagnetic observatories met these criteria: Fürstenfeldbruck (FUR), Europe; Hermanus (HER), South Africa; Langzhou (LZH), China; Alice Springs (ASP), Australia, Tucson (TUC), North America; and Honolulu (HON), North Pacific. Observed responses have also been corrected for the ocean effect using the procedure of Kuvshinov et al. (2002) in an iterative fashion as suggested by Utada et al. (2003). These response functions are mostly sensitive to the depth range $\sim 400-500$ to 1200–1500 km, i.e., lowermost upper mantle, transition-zone, and uppermost lower mantle. Table 3 summarizes geographic and geomagnetic coordinates of the selected observatories and length of data series. Observed responses are shown and discussed further in Sect. 6.4.2.

6.2 Prior Distribution

We consider a spherical Earth whose properties vary laterally and radially, assuming that lateral variations are on longer scale lengths than the depths of penetration of the electromagnetic sounding data. At the location of each geomagnetic observatory (Table 3), we represent a (local) model of the Earth by a number of layers, corresponding to crust and mantle layers. The crust is represented by a local physical model, whereas mantle layers are described by model parameters related to composition and temperature. It is implicitly assumed that all parameters depend on geographical position and depth. Prior information on all parameters is summarized in Table 4 and follows the prior values used in Khan and Shankland (2012).

For the electrical conductivity parameters that appear in Eqs. 5–8 ($\alpha, \alpha_p, \beta, \sigma_o^h, \sigma_o^i, \sigma_o^p, H_i, E_0, V_0, \ldots$), we consider uncertainties in all parameters by assuming that these are uniformly distributed within bounds of $[a - \Delta a; a + \Delta a]$, where a is any of the aforementioned parameters and Δa the associated laboratory-measured/estimated uncertainty. As mentioned earlier, there is no exhaustive attempt to consider other data sets, e.g., measurements by Romano et al. (2006) on garnet, Romano et al. (2009) on hydrous wadsleyite, Poe et al. (2010) and Jones et al. (2012) on hydrous olivine, Wu et al. (2010) on ferropericlase or the databases of Vacher and Verhoeven (2007), Pommier and

Table 3 Summary of geographical and geomagnetic location of observatories and length of data series available for constructing electromagnetic response functions

Station	Latitude (° North)	Longitude (° East)	Geomagnetic latitude (° North)	Observation period
Fürstenfeldbrück (FUR)	48.17	11.28	48.38	1957–2007
Hermanus (HER)	−34.43	19.23	−33.98	1957–2007
Langzhiou (LZH)	36.09	103.85	25.86	1980–2007
Alice Springs (ASP)	−23.76	133.88	−32.91	1992–2007
Tucson (TUC)	32.17	249.27	39.88	1957–1994
Honolulu (HON)	21.32	202.00	21.64	1961–2007

Table 4 Prior information on model parameters

Description	Layers numbers	Parameter	Value/range	Distribution
Crustal thickness	1	d_{Moho}	40 km	Fixed
Crustal conductivity	1	σ_{crust}	10^{-6}–10^{-3} S/m	Uniform
Basalt fraction	2	f	0–1	Log-uniform
				40–410 km depth
				410–2000 km depth
Temperature	25	T	$T_{i-1} \leq T_i \leq T_{i+1}$	Temperature does not decrease with depth
Surface temperature	1	T_{surf}	0 °C	Fixed
Water content (in wt%)	1	$\log_{10}(C_w^{\text{ol}})$	$[-6; -0.82355]$	Log-uniform
	1	$\log_{10}(C_w^{\text{opx}})$	–	Log-uniform but fixed to C_w^{ol} through $D_{\text{H}_2\text{O}}^{\text{opx/ol}}$
	1	$\log_{10}(C_w^{\text{wads}})$	$[-5; 0]$	Log-uniform
	1	$\log_{10}(C_w^{\text{ring}})$	$[-5; 0]$	Log-uniform but fixed to C_w^{wads} through $D_{\text{H}_2\text{O}}^{\text{wads/ring}}$
Water partition coefficient	1	$D_{\text{H}_2\text{O}}^{\text{opx/ol}}$	See Sect. 4.3	Fixed but pressure-dependent
	1	$D_{\text{H}_2\text{O}}^{\text{wads/ring}}$	2	Fixed
Upper mantle water storage capacity	1	$C_{\text{UM}}^{\text{max}}$	0.15 wt%	Fixed
				Pressure-dependent
Melt conductivity	1	$\log_{10}(\sigma_{\text{melt}})$	$[\log_{10}(\sigma_{\text{m}}); 1]$ S/m	Log-uniform
				σ_{m} is conductivity above melt layer
Melt layer thickness	1	d_{melt}	20 km	Fixed
Mantle mineralogy	25	M_i	–	No constraints
Mantle conductivity	25	σ_i	–	No constraints
Core conductivity	1	σ_{core}	$5 \cdot 10^5$ S/m	Fixed

Le Trong (2011), and Karato (2011). Although the choice of experimental data can possibly influence the outcome, this inversion treatment is able to consider uncertainties in measured conductivity parameters and thereby automatically allows for larger variations.

In order to model conductivity of the melt layer, we follow a previous approach (Khan and Shankland 2012) that is based on the physical parameterization of Toffelmier and Tyburczy (2007); they considered conductivities in the range 1–6 S/m as appropriate. These values are based on low-pressure conductivity measurements of basanite melt, olivine tholeiitic melt, "dry" and "wet" rhyolitic melt, Yellowstone rhyolite, and Hawaiian tholeiite (Tyburczy and Waff 1983; Tyburczy and Fisler 1995; Gaillard 2004) and an assumed temperature at 410 km depth of 1420 °C. Thus, we consider a melt layer (where needed) with a fixed thickness of 20 km and conductivity that varies from the "background" mantle value (σ_{m}) to $\sim 10 + \sigma_{\text{m}}$ (in S/m), i.e., $\sigma_{\text{melt}} = \sigma_{\text{m}} + 10\alpha$, where α is a randomly distributed number in the interval 0–1.

In summary, from values of the parameters described above, we compute equilibrium modal mineralogy and bulk conductivity at 75 depth nodes from the surface downward as a

function of pressure, temperature, composition, and water content at intervals of 10 km in the range 40–110 and 570–630 km depth, 20 km in the ranges 110–370, 420–540, and 700–800 km depth, 5 km within the ranges 380–420, 545–570, and 645–700 km depth, 100 km in the range 800–1600 km depth, and finally 200 km in the depth range from 1600 to 2000 km. As there is no unique way to parameterize the model system, the particular parameterization chosen here was found by conducting many trial inversions and reflects a particular, near-minimal, parameterization that yields data fitting the observations within uncertainties. Also, because we neglect uncertainties of measured mineral physics parameters related to the thermodynamic formulation, actual uncertainties are likely to be larger than indicated here.

6.3 Posterior Distribution

On the assumption that data noise can be modeled using a Gaussian distribution and that observational uncertainties and calculation errors between real and imaginary parts of the C-response functions are independent [details on how C-responses are derived is given in Khan et al. (2011)], the likelihood function is given by

$$\mathcal{L}(\mathbf{m}) \propto \exp\left(-\sum_i \frac{\left[{}_i d_{\text{obs}}^{\text{Re}\{C\}} - {}_i d_{\text{cal}}^{\text{Re}\{C\}}(\mathbf{m}) \right]^2}{2 {}_i \Delta_{\text{Re}\{C\}}^2} + \frac{\left[{}_i d_{\text{obs}}^{\text{Im}\{C\}} - {}_i d_{\text{cal}}^{\text{Im}\{C\}}(\mathbf{m}) \right]^2}{2 {}_i \Delta_{\text{Im}\{C\}}^2} \right) \tag{19}$$

where $d_{\text{obs}}^{\text{Re}\{C\}}, d_{\text{obs}}^{\text{Im}\{C\}}, d_{\text{cal}}^{\text{Re}\{C\}}$ and $d_{\text{cal}}^{\text{Im}\{C\}}$ denote observed and calculated real and imaginary C-responses, respectively, and $\Delta_{\text{Re}\{C\}}$ and $\Delta_{\text{Im}\{C\}}$ are the observational uncertainties on either of these.

Sampling proceeded by randomly perturbing either of the 31 parameters $\{f_j, T_i, C_w^{\text{ol}}, C_w^{\text{wads}}, \sigma_{\text{crust}}, \sigma_{\text{melt}}\}$ according to the prior distribution summarized in Table 4. For brevity we leave aside discussion of parameters pertaining to the laboratory conductivity measurements $(\alpha, \alpha_p, \beta, \sigma_o^h, \sigma_o^i, \sigma_o^p, H_i, E_0, V_0, \ldots)$. The burn-in time for this distribution (number of iterations until samples were retained from the posterior distribution) was found to be of the order of 10^4 iterations. We sampled 10 million models, with an overall acceptance rate of about 32 % of which every 200th model was retained for further analysis.

6.4 Results and Discussion

6.4.1 Constraints on Thermochemical Structure of the Mantle

Inverted thermal profiles beneath the six stations are shown in Fig. 7 and suggest lateral and radial variations in mantle thermal structure.[1] Because the C-responses are mainly sensitive to the base of the upper mantle, transition zone, and upper part of the lower mantle, we only show models in the depth range 300–1200 km. The geotherms remain relatively well-defined over most of the depth range shown with some broadening below 1000 km depth (HER and HON). The geotherms span mantle temperatures in the range

[1] Inverted compositional profiles are not shown here for brevity. However, the compositional variations found here are relatively large spanning basalt fractions that range in excess of 0.2 or more. What can be inferred with relative certainty, though, is a radial increase in basalt fraction with depth.

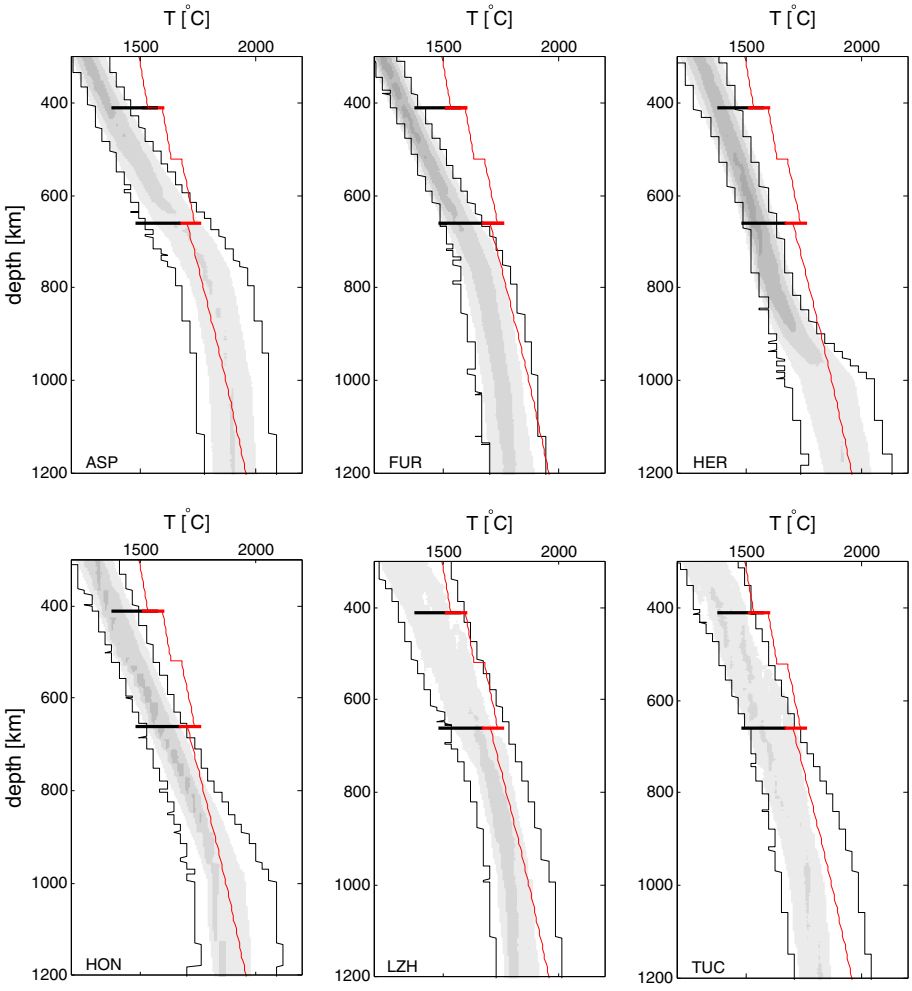

Fig. 7 Sampled thermal profiles beneath stations ASP, FUR, HER, HON, LZH, and TUC (observatories are defined in Sect. 6.1). The contoured profiles are related directly to their probability of occurrence. The *contour lines* define 20 equal-sized probability density intervals for the distributions (*black most probable* and *white least probable*). *Black* and *red horizontal bars* indicate experimentally determined temperatures for the major mineral phase reactions at 410 and 660 km depth by Ito and Takahashi (1989) and Katsura et al. (2010), respectively. The adiabatic temperature profile of Katsura et al. (2010) is shown in *red*. *Thin solid black lines* indicate 95 % posterior credible intervals of sampled thermal models

150−200 °C that increase to 250−300 °C below. These results generally agree with the earlier determinations by Khan and Shankland (2012) for stations ASP, FUR, LZH and TUC. Given modeling differences and changes to the conductivity database, this observation suggests that inverting long-period C-responses directly for mantle temperature is fairly robust.

For comparison, experimentally determined temperatures at which mineral phase transitions in the system $(Mg,Fe)_2SiO_4$ have been observed are also shown in Fig. 7. Ito and Takahashi (1989), for example, found that the ol → wads and ring → fp + br

reactions occurred at temperatures of $\sim 1750 \pm 100$ K and $\sim 1900 \pm 150$ K, respectively, whereas Katsura et al. (2004) obtained temperatures of 1760 ± 45 K and 1860 ± 50 K for the same reactions. Also shown in Fig. 7 is the adiabatic temperature profile of Katsura et al. (2010). Discrepancies between the adiabat of Katsura et al. (2010) and inverted mantle temperatures here have to be viewed in the light of differences in composition. The compositions investigated here span a much larger range than the single composition (peridotite) investigated by Katsura et al. (2010).

In summary, there appears to be good evidence for lateral and radial variations in both mantle temperature and composition, although it should be noted that the results presented here depend on the particular conductivity data set employed. Nevertheless, the results support the concept of distinct end-member compositions (e.g., Xu et al. 2008) resulting from asthenospheric melting.

6.4.2 Constraints on Conductivity Structure

Laboratory-based conductivity profiles computed from the inverted thermo-chemical profiles and the conductivity database outlined in Sect. 4.1 are shown in Fig. 8. Calculated and observed long-period inductive response functions are compared in Fig. 9. Several features of the conductivity profiles appears to be consistent. Most prominently among these are the following:

- Averaged conductivity profiles beneath the various stations generally correlate with temperature structure;
- Only the profiles beneath stations LZH and TUC show presence of high-conductivity layers just above the transition zone;
- Absence of conductivity jumps across the olivine→wadsleyite transformation. This contrasts with earlier laboratory-based profiles of, e.g., Xu et al. (2000) and Karato (2011), who found strong increases in conductivity around the "410-km" discontinuity due to the use of different conductivity data that were based, in the case of Xu et al. (2000), on earlier measurements of anhydrous minerals;
- Lateral variations within the transition zone. Profiles beneath HER/HON appear to display the most "structure", including relatively prominent discontinuities associated with the wadsleyite → ringwoodite phase transition (the "520-km" discontinuity);
- Strong lateral variations in the structure of the "660-km" discontinuity. Beneath FUR the "660-km" appears to be sharp, whereas beneath LZH/TUC the "660-km" could be characterized as sharp-to-gradual, and underneath ASP/HER/HON the "660-km" is clearly gradual and depressed relative to the other locations;
- The structure of the "660-km" discontinuity is found to correlate with the compositional variations within the transition zone that are also apparent in Fig. 1: the profiles with gradual and sharp-to-gradual as well as depressed discontinuities are characterized by high basalt fractions (~ 0.5–0.8), i.e., more MORB-like, whereas a sharp conductivity jump around 660 km depth is indicative of relatively low basalt fractions (~ 0.2), i.e., more harzburgitic. This possibly indicates that transition-zone topography bears a compositional imprint;
- General overlap between the various profiles in the lower mantle (800–1200 km depth), implying transition to a structurally homogeneous lower mantle.

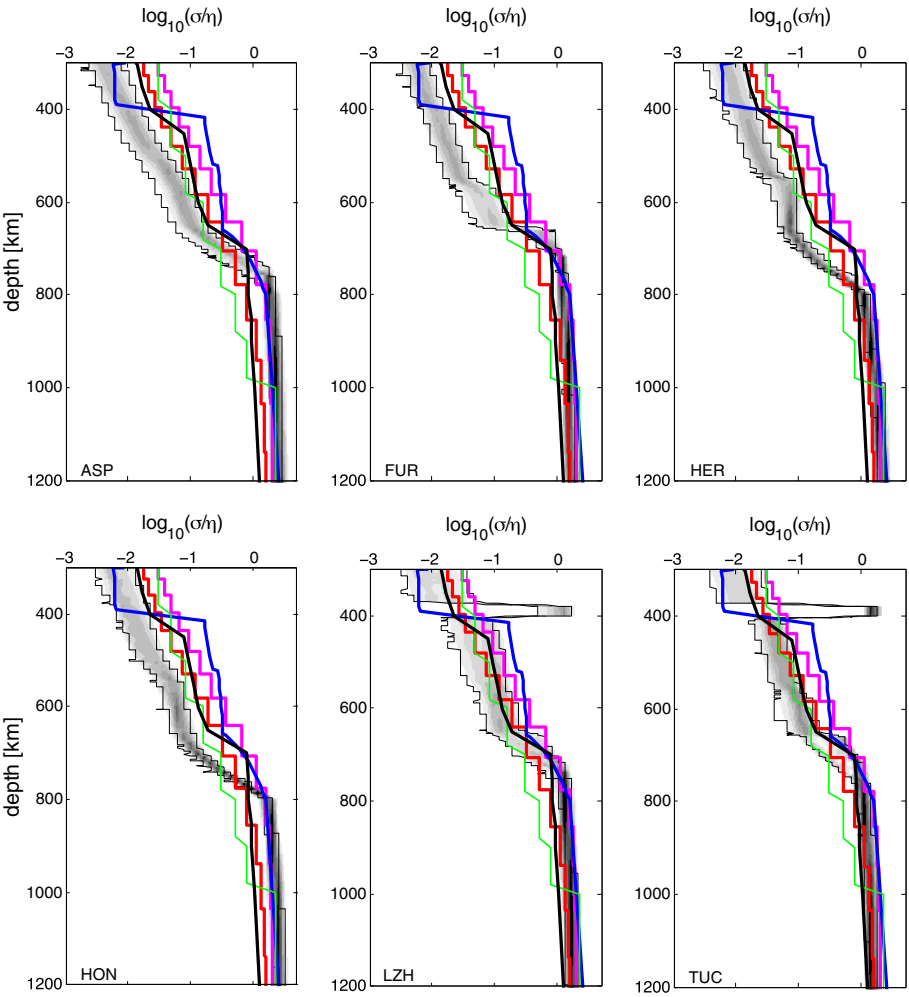

Fig. 8 Sampled electrical conductivity profiles beneath stations ASP, FUR, HER, HON, LZH, and TUC (observatories are defined in Sect. 6.1). The contoured profiles are related directly to their probability of occurrence. The *contour lines* define 20 equal-sized probability density intervals for the distributions (*black most probable* and *white least probable*). *Thin black lines* indicate 95 % credible intervals of sampled conductivity models. For comparison field-derived one-dimensional conductivity profiles are also shown (*bold lines*): Olsen (1999, *red*); Kuvshinov and Olsen (2006, *magenta*); Velimský (2010, *green*); Xu et al. (2000, *blue*); Khan et al. (2006, *black*); Note that the model of Khan et al. (2006) represents their mean profile. $\eta = 1$ S/m

The regional variations observed here are supported by previous geophysically derived 1-D models. Unlike the profiles presented here that implicitly incorporate discontinuities across major phase transitions, the subcontinental European conductivity model of Olsen (1999) and global models of Kuvshinov and Olsen (2006) and Velimský (2010) are all characterized by a continuous conductivity increase through the mantle. This results from the diffusive nature of electromagnetic fields that renders these insensitive to

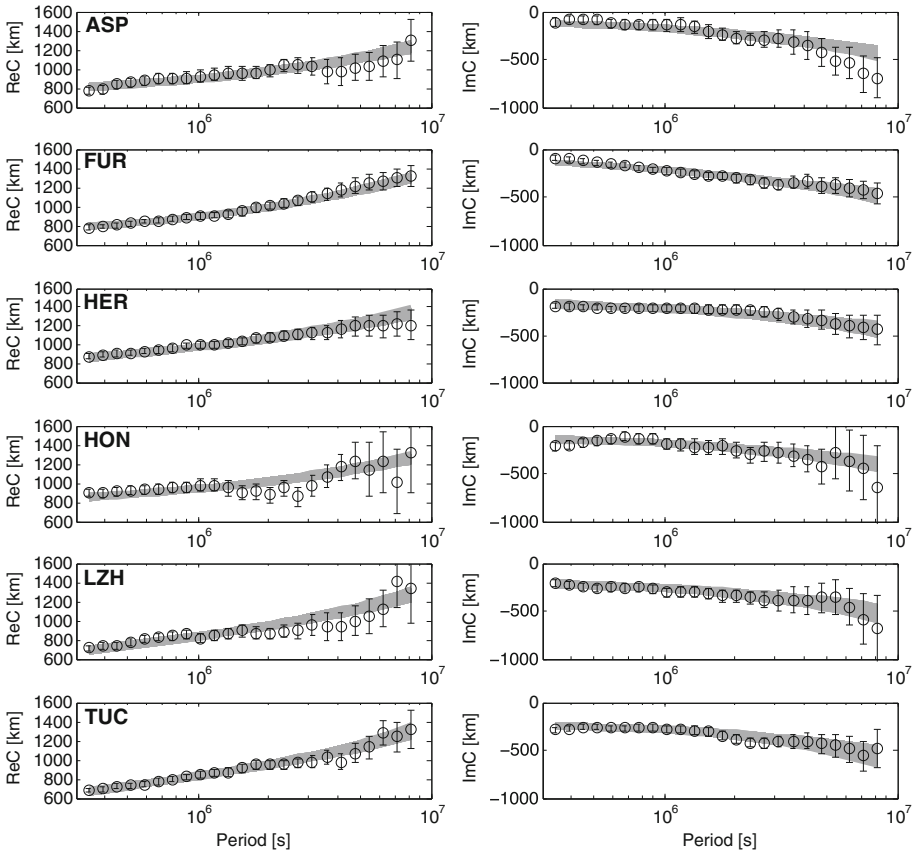

Fig. 9 Fit to inductive response functions (observed data—*circles*) and uncertainties (*bars*) from six geomagnetic observatories using the conductivity profiles in Fig. 8 (*shaded bands*—calculated data). *Left* and *right columns* depict real and imaginary parts of C-responses, respectively. For station details see Sect. 6.1 and Table 3

discontinuities, although evidence for a strong change in conductivity around 410 km depth and shallower has been reported (e.g., Schultz et al. 1993; Simpson 2001).

As observed earlier (Khan et al. 2011; Khan and Shankland 2012), the non-monotonic increase in the real part of the observed C-responses at stations ASP, HON, and LZH (Fig. 9) appear to be incompatible with the assumption of a 1-D conductivity structure (Weidelt 1972). There are three possible reasons for this non-monotonic data behavior: the assumed P_0^1 source structure is violated, core contamination is present in the signal within the observed period range, and/or three-dimensional conductivity effects could be influencing the C-responses. Comparison of C-responses based on one-dimensional and three-dimensional models (constructed by interpolating profiles obtained from inversion of 1D models), showed little difference (Khan et al. 2011). We also note that for stations ASP, HON, and LZH uncertainties increase significantly at longer periods. This is directly related to a shorter time span over which data were collected.

6.4.3 Constraints on Mantle Water Content

Sampled water contents in major upper mantle[2] and transition-zone minerals olivine (C_w^{ol}) and wadsleyite (C_w^{wads}) are shown in Fig. 10. Generally, we find that $C_w^{ol} < 0.02$ wt% underneath most of the stations, with typical values around 0.01 wt% H_2O, except for one station (FUR) where $C_w^{ol} \sim 0.02$–0.04 wt%. This indicates a relatively dry upper mantle in agreement with earlier findings that considered two different conductivity databases (e.g., Khan and Shankland 2012), compilations of other data sets (e.g., Fullea et al. 2011; Jones et al. 2012), and not least water contents inferred from analysis of natural samples as discussed earlier (e.g., Peslier and Bizmis 2015).

Although there is fairly good agreement between these various estimations, it should be kept in mind that the long-period inductive responses inverted here are mainly sensitive in the depth range 400–1200 km (Khan et al. 2011; Püthe et al. 2015). This implies that resolution of upper mantle water content is limited.[3] Other data based on either magnetotellurics or shorter-period inductive response functions related to S_q variations are needed to infer the conductivity structure of the upper mantle proper ($\sim 50-400$ km) (e.g., Samrock and Kuvshinov 2013; Koch and Kuvshinov 2013).

As expected, the water content of the transition zone is, based on experimental observations of the water storage capacity of transition-zone minerals wadsleyite and ringwoodite (e.g., Bolfan-Casanova 2005; Hirschmann 2006; Pearson et al. 2014), higher than that of olivine and thus of the upper mantle in general. C_w^{wads} ranges from ~ 0.1 wt% H_2O to ~ 1 wt% H_2O. The sampled distributions (Fig. 10) are clearly distinct and point to lateral variations in transition-zone water content that appear to be locally elevated underneath two locations (TUC and LZH).

6.4.4 Implications for Mantle Melting

Conductivities beneath two of the investigated stations (TUC and LZH) were found to be relatively high, ranging from $\sim 0.6-1.6$ S/m (LZH) to $\sim 1.2-2$ S/m (TUC), respectively. For comparison, background mantle conductivities above and below are ~ 2 orders of magnitude less. This can result from elevated hydration levels (> 0.15 wt%) within the transition zone beneath these two stations; such high water concentrations exceed the assumed maximum upper mantle water storage capacity (0.15 wt% H_2O). From the physical parameterization of mantle water content, storage capacity, and melt conductivity adopted here (cf. Sect. 5.1.2), this suggests that water-rich material advected from the transition zone and into the base of the upper mantle beneath the two stations has undergone hydration melting with melt appearing on top of the "410-km" discontinuity.

In evaluating the requirements for the presence of melt in this region, accurate constraints on the H_2O storage capacity of the deep upper mantle are necessary. We tested the robustness of the results by lowering the maximum water storage capacity of the upper mantle to 0.1 wt%. We reperformed the inversions with this new constraint for the storage

[2] Water content in orthopyroxene and ringwoodite is fixed through the use of the partition coefficients $D_{H_2O}^{opx/ol}$ and $D_{H_2O}^{ring/wads}$ (see Table 4).

[3] This observation was partly confirmed in an inversion of the C-responses for station TUC where we inverted for C_w^{ol} and C_w^{opx} separately, i.e., without reference to $D_{H_2O}^{opx/ol}$, and found little change relative to the results presented here. On the other hand, this also shows that, because of the small amounts of opx present, application of $D_{H_2O}^{opx/ol}$ is relatively insignificant.

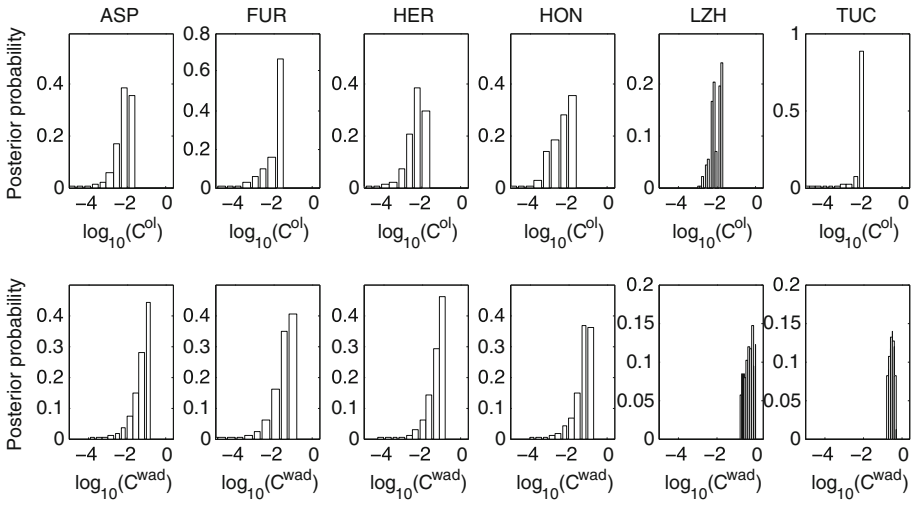

Fig. 10 Sampled water content in major upper mantle and transition-zone minerals olivine (C_w^{ol}) and wadsleyite (C_w^{wads}). Water content is given in terms of $C^x = C_w^x / C_w^0$, where x denotes either of the minerals. C_w^x is in wt% and $C_w^0 = 1$ wt%

capacity of the upper mantle, but found no significant changes. The new results imply no additional melt layers at the other locations. With regard to the conductivity database, Khan and Shankland (2012) showed that use of another conductivity database also resulted in melt at the base of the mantle underneath station LZH. This suggests that these features are fairly robust within the accuracy of the experimental observations and that melt layers are more likely to be local/regional than a global phenomenon as proposed by Bercovici and Karato (2003).

Observing the presence of melt in the C-responses is admittedly more difficult, and we should note that models without melt are also able to fit data as shown in Khan et al. (2011). The current inference of melt therefore has to be viewed in the context of the water-melt model, which is based on a physical parameterization of the behavior of water-induced melting as observed experimentally and supplemented with laboratory measurements of silicate melt conductivity (cf. Sect. 5.1.2). Thus, although data might not be able to accurately resolve a thin melt layer, physical conditions are such that melt can be expected to stabilize.

7 Concluding Remarks

It has been the purpose here to present a methodology for making quantitative inferences about the constitution and interior structure of the Earth from geophysical, geochemical, and petrological data. Central to the approach is the inversion of geophysical data directly for the fundamental parameters of interest (mantle chemical composition and temperature). The postulate is that a quantitative approach in which geophysical data are tested directly for fundamental parameters should be emphasized over approaches that rely on qualitative comparison between geophysical models and forward models constructed from laboratory measurements.

The connection between geophysical observables, physical rock properties (electrical conductivity), and material properties (thermo-chemical state) is provided by thermodynamics of mantle minerals. Through the use of a self-consistent thermodynamic modeling scheme of mantle mineral phase equilibria that depend only on composition, temperature, and pressure, we are able to compute all relevant thermodynamic properties. The great advantage of this approach is that it inserts plausible petrological and geochemical knowledge directly in the form of data and/or prior information into the geophysical inverse problem that would not be possible in traditional inversion of geophysical data (here electromagnetic sounding data) for physical rock properties. Incorporation of experimental petrological data has been illustrated with the use of water partition coefficients and water storage capacities of the main minerals that make up the mantle. These parameters describe how water is divided between the various mineral phases and the maximum amount of water that each of these can hold without giving rise to a hydrous melt. Consideration of partition coefficients is important inasmuch as it allows for internally consistent modeling of the water distribution between the major minerals. Moreover, mantle mineral phase equilibria fundamentally help to resolve discontinuities that straightforward inversion of electromagnetic sounding data is incapable of "seeing" in spite of the fact that these are present.

The methodology has been illustrated with a specific example where we inverted a set of long-period electromagnetic sounding data beneath six geomagnetic stations directly for the physico-chemical structure of the mantle (major element composition, water content, and thermal state). The inversion can produce conductivity profiles that fit geophysical data within uncertainties to obtain models of mantle conditions that simultaneously combine features of both laboratory and geophysical data. The results indicate that the thermo-chemical state of the mantle can be reasonably well-retrieved given a set of high-quality inductive response functions and a specific set of measurements of laboratory mineral conductivity and water partition coefficients and saturation levels.

Like other methods, this integrated approach leads to further work. Of main importance are (1) continued collection and refinement of the laboratory-based mineral conductivity database, particularly an improved conductivity database for all major hydrous upper mantle, transition zone, and lower-mantle minerals; (2) improved understanding of the partitioning behavior of water between mantle minerals and melt; (3) continued effort to extend the thermodynamic database employed in computing mantle mineral phase equilibria so as to model effects related to oxygen fugacity, water, and presence of melt; and (4) construction of high-quality inductive response functions (or more generally geophysical data) of high coherency and small uncertainties. As the various data sets become available or continue to be refined, these can, because of the general formulation of the methodology, be incorporated in a straightforward manner.

Because of their versatility, integrated approaches are becoming more popular with the geoscience community and cover a wide range of applications, including seismology, gravity, electromagnetics, topography, and petrology, that are performed either in a predictive sense (e.g., Sobolev and Babeyko 1994; Dobson and Brodholt 2000b; Fukao et al. 2004; Utada et al. 2009; Ritsema et al. 2009; Fullea et al. 2014; Kuskov et al. 2014; Kaban et al. 2014) or in an inverse sense (e.g., Shapiro and Ritzwoller 2004; Khan et al. 2013; Cobden et al. 2008; Afonso et al. 2013a, b; Drilleau et al. 2013).

Acknowledgments I would like to extend my gratitude to Thomas Shankland for helpful comments throughout and for proofreading the final manuscript. Many thanks also to Ian Ferguson and three

anonymous reviewers for critically reviewing the manuscript. Finally, I would like to acknowledge Nathalie Bolfan-Casanova, Konstantin Litasov, and Shun Karato for sharing their figures.

References

Afonso JC, Fullea J, Yang Y, Connolly JAD, Jones AG (2013a) 3D multi-observable probabilistic inversion for the compositional and thermal structure of the lithosphere and upper mantle. II: General methodology and resolution analysis. J Geophys Res 118:1650. doi:10.1002/jgrb.50123

Afonso JC, Fullea J, Griffin WL, Yang Y, Jones AG, Connolly JAD, OReilly SY (2013b) 3D multi-observable probabilistic inversion for the compositional and thermal structure of the lithosphere and upper mantle. I: a priori petrological information and geophysical observables. J Geophys Res 118:1. doi:10.1002/jgrb.50124

Afonso JC, Fernandez M, Ranalli G, Griffin WL, Connolly JAD (2008) Combined geophysical-petrological modelling of the lithospheric-sublithospheric upper mantle: methodology and applications. Geochem Geophys Geosyst 9:Q05008. doi:10.1029/2007GC001834

Afonso JC, Zlotnik S, Díez P (2015) An efficient and general approach for implementing thermodynamic phase equilibria information in geophysical and geodynamic studies. Geochem Geophys Geosyst 16:3767–3777. doi:10.1002/2015GC006031

Ardia P, Hirschmann MM, Withers AC, Tenner TJ (2012) H_2O storage capacity of olivine at 5–8 GPa and consequences for dehydration partial melting of the upper mantle. Earth Planet Sci Lett 345:104

Aubaud C, Hauri EH, Hirschmann MM (2004) Hydrogen partition coefficients between nominally anhydrous minerals and basaltic melts. Geophys Res Lett 31:L20611. doi:10.1029/2004GL021341

Baba K, Chave AD, Evans RL, Hirth G, Mackie RL (2006) Mantle dynamics beneath the East Pacific Rise at 17 degrees S: insights from the Mantle Electromagnetic and Tomography (MELT) experiment. J Geophys Res 111. doi:10.1029/2004jb003598

Baba K, Utada H, T-n G, Kasayac T, Shimizua H, Tada N (2010) Electrical conductivity imaging of the Philippine Sea upper mantle using seafloor magnetotelluric data. Phys Earth Planet Int 183:44. doi:10.1016/j.pepi.2010.09.010

Ballhaus C (1995) Is the upper mantle metal-saturated? Earth Planet Sci Lett 132:75

Banks RJ (1969) Geomagnetic variations and the electrical conductivity of the upper mantle. Geophys J R Astron Soc 17:457

Becken M, Ritter O (2012) Magnetotelluric studies at the San Andreas Fault zone: implications for the role of fluids. Surv Geophysics 33:65. doi:10.1007/s10712-011-9144-0

Bell DR, Rossmann GR (1992) Water in Earth's mantle: the role of nominally anhydrous minerals. Science 255:1391

Bercovici D, Karato S-I (2003) Whole-mantle convection and the transition-zone water filter. Nature 425:39

Berryman JG (1995) Mixture theories for rock properties. In: Ahrens TJ (ed) American geophysical union handbook of physical constants 205. AGU, New York

Bina CR (1998) Free energy minimization by simulated annealing with applications to lithospheric slabs and mantle plumes. Pure Appl Geophys 151:605

Bolfan-Casanova N (2005) Water in the Earth's mantle. Min Mag 69:227

Bolfan-Casanova N, Keppler H, Rubie DC (2000) Partitioning of water between mantle phases in the system $MgOGSiO_2H_2O$ up to 24 GPa: implications for the distribution of water in the Earth's mantle. Earth Planet Sci Lett 182:209

Bolfan-Casanova N, McCammon CA, Mackwell SJ (2006) Water in transition zone and lower mantle minerals. In: Jacobsen SD, van der Lee S (eds) Earth's deep water cycle geophysical monograph series, 168. AGU, New York. doi:10.1029/168GM06

Brown JM, Shankland TJ (1981) Thermodynamic parameters in the Earth as determined from seismic profiles. Geophys J Roy Astron Soc 66:579

Chen J, Inoue T, Yurimoto H, Weidner DJ (2002) Effect of water on olivine wadsleyite phase boundary in the $(Mg,Fe)_2SiO_4$ system. Geophys Res Lett 29:1875. doi:10.1029/2001GL014429

Cobden L, Goes S, Cammarano F, Connolly JAD (2008) Thermochemical interpretation of one-dimensional seismic reference models for the upper mantle: Evidence for bias due to heterogeneity. Geophys J Int 175:417. doi:10.1111/j.1365-246X.2008.03903.x

Connolly JAD (2009) The geodynamic equation of state: What and how. Geophys Geochem Geosys 10:Q10014. doi:10.1029/2009GC002540

Dai L, Li H, Hu H, Shan S (2008) Experimental study of grain boundary electrical conductivities of dry synthetic peridotite under high-temperature, high-pressure, and different oxygen fugacity conditions. J Geophys Res 113:B12211. doi:10.1029/2008JB005820
Dasgupta R, Hirschmann MM (2010) The deep carbon cycle and melting in Earths interior. Earth Planet Sci Lett 298:1
Davies G (2006) Gravitational depletion of the earthly Earths upper mantle and the viability of early plate tectonics. Earth Planet Sci Lett 243:376. doi:10.1016/j.epsl.2006.01.053
Deon F, Koch-Müller M, Rhede D, Wirth R (2011) Water and iron effect on the P-T-x coordinates of the 410-km discontinuity in the Earth's upper mantle. Contrib Min Petrol. doi:10.10007/s00410-010-0555-6
Demouchy S, Deloule E, Frost DJ, Keppler H (2005) Pressure and temperature-dependence of water solubility in iron-free wadsleyite. Am Mineralog 90:1084
Dobson DP, Brodholt JP (2000a) The electrical conductivity of the lower mantle phase magnesiowüstite at high temperatures and pressures. J Geophys Res 105:531
Dobson DP, Brodholt JP (2000b) The electrical conductivity and thermal profile of the Earth's mid-mantle. Geophys Res Lett 27:2325
Drilleau M, Beucler E, Mocquet A, Verhoeven O, Moebs G, Burgos G, Montagner JP, Vacher P (2013) A Bayesian approach to infer radial models of temperature and anisotropy in the transition zone from surface wave data. Geophys J Int. doi:10.1093/gji/ggt284
Du Frane WL, Roberts JJ, Toffelmier DA, Tyburczy JA (2005) Anisotropy of electrical conductivity in dry olivine. Geophys Res Lett 32:L24315. doi:10.1029/2005GL023879
Duba A (1982) Limits to electrical measurements of silicates. In: Schreyer W (ed) High-pressure researches in geosciences. Schweizerbartische Verlagsbuchhandlung, Stuttgart, p 375381
Duba A, Shankland TJ (1982) Free carbon and electrical conductivity in the earths mantle. Geophys Res Lett 9:1271
Duba AG, Constable S (1993) The electrical conductivity of lherzolite. J Geophys Res 98:11885
Ducea MN, Park SK (2000) Enhanced conductivity from sulfide minerals, southern Sierra Nevada, California. Geophys Res Lett 27:2405. doi:10.1029/2000GL011565
Evans RL, Hirth G, Baba K, Forsyth D, Chave A, Mackie R (2005) Geophysical evidence from the MELT area for compositional controls on oceanic plates. Nature 437:249
Fabrichnaya OB (1999) The phase relations in the $Al_2O_3-SiO_2$ system: Assessment of thermodynamic properties and phase equilibria at pressures up to 30 GPa. Calphad 23:19
Férot A, Bolfan-Casanova N (2012) Water storage capacity in olivine to 14 GPa and implications for the water content of the Earth's upper mantle. Earth Planet Sci Lett 349–350:218. doi:10.1016/j.epsl.2012.06.022
Frost DJ (2003) The structure and sharpness of $(Mg,Fe)_2SiO_4$ phase transformations in the transition zone. Earth Planet Sci Lett 216:313
Frost DJ, Dolejs D (2007) Experimental determination of the effect of H_2O on the 410-km seismic discontinuity. Earth Planet Sci Lett 256:182
Frost DJ, McCammon CA (2008) The redox state of the Earths mantle. Annu Rev Earth Planet Sci 36:389
Frost DJ, Liebske C, Langenhorst F, McCammon CA, Trónnes RG, Rubie DC (2004) Experimental evidence for the existence of iron-rich metal in the Earth's lower mantle. Nature 428:409
Fukao Y, Koyama T, Obayashi M, Utada H (2004) Trans-Pacific temperature field in the mantle transition region derived from seismic and electromagnetic tomography. Earth Planet Sci Lett 217:425
Fullea J, Muller MR, Jones AG (2011) Electrical conductivity of continental lithospheric mantle from integrated geophysical and petrological modeling: application to the Kaapvaal Craton and Rehoboth Terrane, southern Africa. J Geophys Res 116:B10202. doi:10.1029/2011JB008544
Fullea J, Lebedev S, Agius MR, Jones AG, Afonso JC (2012) Lithospheric structure in the Baikal-central Mongolia region from integrated geophysical-petrological inversion of surface-wave data and topographic elevation. Geochem Geophys Geosys 13:Q0AK09. doi:10.1029/2012GC004138
Fullea J, Muller MR, Jones AG, Afonso JC (2014) The lithosphere-asthenosphere system beneath Ireland from integrated geophysical-petrological modeling - II: 3D thermal and compositional structure. Lithos 189:49. doi:10.1016/j.lithos.2013.09.014
Gaillard F (2004) Laboratory measurements of electrical conductivity of hydrous and dry silicic melts under pressure. Earth Planet Sci Lett 218:215. doi:10.1016/S0012-821X(03)00639-3
Gaillard F, Marki M, Iacono-Marziano G, Pichavant M, Scaillet B (2008) Carbonatite melts and electrical conductivity in the asthenosphere. Science 32:1363
Gardés E, Gaillard F, Tarits P (2015) Toward a unified hydrous olivine electrical conductivity law. Geochem Geophys Geosyst 15:4984. doi:10.1002/2014GC005496

Ghosh S, Ohtani E, Litasov KD, Suzuki A, Dobson D, Funkoshi K (2013) Effect of water in depleted mantle on post-spinal transition and implication for 660 km seismic discontinuity. Earth Planet Sci Lett 371–372:103. doi:10.1016/j.epsl.2013.04.011

Guo X, Yoshino T (2013) Electrical conductivity of dense hydrous magnesium silicates with implication for conductivity in the stagnant slab. Earth Planet Sci Lett 369–370:239. doi:10.1016/j.epsl.2013.03.026

Hashin Z, Shtrikman S (1962) A variational approach to the theory of effective magnetic permeability of multiphase materials. J Appl Phys 33:3125

Hastings WK (1970) Monte Carlo sampling methods using Markov chains and their applications. Biometrika 57:97

Hauri EH, Gaetani GA, Green TH (2006) Partitioning of water during melting of the Earth"s upper mantle at H_2O—undersaturated conditions. Earth Planet Sci Lett 248:715

Helffrich GR (2002) Chemical and seismological constraints on mantle heterogeneity. Philos Trans R Soc London Ser A 360:2493. doi:10.1098/rsta.2002.1085

Helffrich GR (2006) Heterogeneity in the mantle-Its creation, evolution and destruction. Tectonophysics 416:23. doi:10.1016/j.tecto.2005.11.012

Helffrich GR, Wood BJ (2001) The Earth's mantle. Nature 412:501. doi:10.1038/35087500

Hill R (1963) The elastic behaviour of crystalline aggregate. J Mech Phys Solids 11:357

Hirschmann MM (2006) Water, melting, and the deep Earth H_2O cycle 34:629. doi:10.1146/annurev.earth.34.031405.125211

Hirschmann MM (2010) Partial melt in the oceanic low velocity zone. Phys Earth Planet Int 179:60

Hirschmann MM, Aubaud C, Withers AC (2005) Storage capacity of H_2O in nominally anhydrous minerals in the upper mantle. Earth Planet Sci Lett 236:167

Hirschmann MM, Tenner T, Aubaud C, Withers AC (2009) Dehydration melting of nominally anhydrous mantle: the primacy of partitioning. Phys Earth Planet Int 176:54. doi:10.1016/j.pepi.2009.04.001

Hirth G, Kohlstedt DL (1996) Water in the oceanic upper mantle: implications for rheology, melt extraction and the evolution of the lithosphere. Earth Planet Sci Lett 144:93

Hofmann AW (1997) Mantle geochemistry: the message from oceanic volcanism. Nature 385:219. doi:10.1038/385219a0

Huang X, Xu Y, Karato S-I (2005) Water content in the transition zone from electrical conductivity of wadsleyite and ringwoodite. Nature 434:746

Inoue T, Yurimoto H, Kudoh Y (1995) Hydrous modified spinel, $MgSiO_4$, a new water reservoir in the mantle transition zone. Geophys Res Lett 22:117

Inoue T, Wadaa T, Sasakia R, Yurimoto H (2010) Water partitioning in the Earths mantle. Phys Earth Planet Int 183:245. doi:10.1016/j.pepi.2010.08.003

Irifune T (1994) Absence of an aluminous phase in the upper part of the Earths lower mantle. Nature 370:131

Ito E, Takahashi E (1989) Postspinal transformations in the system Mg_2SiO_4−Fe_2SiO_4 and some geophysical implications. J Geophys Res 94:10637

Ji S, Wang Q, Xia B, Marcotte D (2004) Mechanical properties of multiphase materials and rocks: a phenomenological approach using generalized means. J Struct Geol 26:1377

Jones AG, Evans RL, Eaton DW (2009) Velocity-conductivity relationships for mantle mineral assemblages in Archean cratonic lithosphere based on a review of laboratory data and Hashin-Shtrikman extremal bounds. Lithos 109:131. doi:10.1016/j.lithos.2008.10.014

Jones AG, Fullea J, Evans RL, Muller MR (2012) Water in cratonic lithosphere: calibrating laboratory-determined models of electrical conductivity of mantle minerals using geophysical and petrological observations. Geochem Geophys Geosyst 13:Q06010. doi:10.1029/2012GC004055

Jones AG (2014) Reconciling different equations for proton conduction using the Meyer-Neldel compensation rule. Geochem Geophys Geosyst 15:337. doi:10.1002/2013GC004911

Jones AG, Afonso JC, Fullea J, Salajegheh F (2014) The lithosphere-asthenosphere system beneath Ireland from integrated geophysical-petrological modelling I: observations, 1D and 2D hypothesis testing. Lithos 189:28. doi:10.1016/j.lithos.2013.10.033

Kaban MK, Tesauro M, Mooney MD, Cloetingh SAPL (2014) Density, temperature, and composition of the North American lithosphere-New insights from a joint analysis of seismic, gravity, and mineral physics data: 1. Density structure of the crust and upper mantle. Geochem Geophys Geosyst 15:4781. doi:10.1002/2014GC005483

Karato S-I (1990) The role of hydrogen in the electrical conductivity of the upper mantle. Nature 347:272

Karato S-I (2011) Water distribution across the mantle transition zone and its implications for global material circulation. Earth Planet Sci Lett 301:413. doi:10.1016/j.epsl.2010.11.038

Karato S-I, Dai L (2009) Comments on Electrical conductivity of wadsleyite as a function of temperature and water content by Manthilake et al. Phys Earth Planet Int. doi:10.1016/j.pepi.2009.01.011

Karato S-I, Wang D (2013) Electrical conductivity of minerals and rocks. In: Karato S (ed) Physics and chemistry of the deep earth. Wiley-Blackwell, New York 145

Katsura T, Yamada H, Kubo A, Shinmei T, Nishikawa O, Yoshino T, Aizawa Y, M-s S, Walter MJ, Ito E, Funakoshi K (2004) Olivine-wadsleyite transition in the system $(Mg,Fe)_2SiO_4$. J Geophys Res 109:B02209. doi:10.1029/2003JB002438

Katsura T, Yokoshi S, Kawabe K, Shatskiy A, Okube M, Fukui H, Ito E, Nozawa A, Funakoshi K (2007) Pressure dependence of electrical conductivity of (Mg,Fe) SiO_3 ilmenite. Phys Chem Miner 34:249

Katsura T, Yoneda A, Yamazaki D, Yoshino T, Ito E (2010) Adiabatic temperature profile in the mantle. Phys Earth Planet Int 183. doi:10.1016/j.pepi.2010.07.001

Kawamoto T, Hervig RL, Holloway JR (1996) Experimental evidence for a hydrous transition zone in the early Earth's mantle. Earth Planet Sci Lett 142:587

Kelbert A, Schultz A, Egbert G (2009) Global electromagnetic induction constraints on transition-zone water content variations. Nature 460. doi:10.1038/nature08257

Keppler H, Bolfan-Casanova N (2006) Thermodynamics of water solubility and partitioning. Rev Mineral Geochem Min Soc Am 62:193

Khan A, Shankland TJ (2012) A geophysical perspective on mantle water content and melting: inverting electromagnetic sounding data using laboratory-based electrical conductivity profiles. Earth Planet Sci Lett 317318:27

Khan A, Connolly JAD, Olsen N (2006) Constraining the composition and thermal state of the mantle beneath Europe from inversion of long-period electromagnetic sounding data. J Geophys Res 111:B10102. doi:10.1029/2006JB004270

Khan A, Connolly JAD, Maclennan J, Mosegaard K (2007) Joint inversion of seismic and gravity data for lunar composition and thermal state. Geophys J Int 168:243. doi:10.1111/j.1365-246X.2006.03200.x

Khan A, Boschi L, Connolly JAD (2009) On mantle chemical and thermal heterogeneities and anisotropy as mapped by inversion of global surface wave data. J Geophys Res 114:B09305. doi:10.1029/2009JB006399

Khan A, Kuvshinov A, Semenov A (2011) On the heterogeneous electrical conductivity structure of the Earth's mantle with implications for transition zone water content. J Geophys Res 116:B01103. doi:10.1029/2010JB007458

Khan A, Zunino A, Deschamps F (2013) Mantle thermochemical and anisotropic variations imaged beneath Australia from Bayesian inversion of surface-wave phase velocities. J Geophys Res 118. doi:10.1002/jgrb.50304

Khan A, Connolly JAD, Pommier A, Noir J (2014) Geophysical evidence for melt in the deep lunar interior and implications for lunar evolution. J Geophys Res Planets 119. doi:10.1002/2014JE004661

Koch S, Kuvshinov A (2013) Global 3-D EM inversion of Sq variations based on simultaneous source and conductivity determination: concept validation and resolution studies. Geophys J Int 195:98. doi:10.1093/gji/ggt227

Kohlstedt DL, Keppler H, Rubie DC (1996) Solubility of water in the α, β, γ phases of $(Mg,Fe)_2SiO_4$. Contrib Mineral Petrol 123:345

Koyama T, Shimizu H, Utada H, Ichiki M, Ohtani E, Hae R (2006) Water content in the mantle transition zone beneath the north Pacific derived from the electrical conductivity anomaly. In: Jacobsen SD, van der Lee S (eds) Earths deep water cycle, AGUGeophysicalMonograph, vol 168. American Geophysical Union, p 171179

Koyama T, Khan A, Kuvshinov A (2014) Three-dimensional electrical conductivity structure beneath Australia from inversion of geomagnetic observatory data: evidence for lateral variations in transition-zone temperature, water content and melt. Geophys J Int. doi:10.1093/gji/ggt455

Kuskov OL, Kronrod VA, Prokofyev AA, Pavlenkova NI (2014) Thermo-chemical structure of the lithospheric mantle underneath the Siberian craton inferred from long-range seismic profiles. Tectonophysics 615–616:154. doi:10.1016/j.tecto.2014.01.00

Kustowski B, Ekstrom G, Dziewonski AM (2008) Anisotropic shear-wave velocity structure of the Earth's mantle: a global model. J Geophys Res 113:B06306. doi:10.1029/2007JB005169

Kuvshinov A, Olsen N (2006) A global model of mantle conductivity derived from 5 years of CHAMP, rsted, and SACC magnetic data. Geophys Res Lett 33:L18301. doi:10.1029/2006GL027083

Kuvshinov AV, Olsen N, Avdeev DB, Pankratov OV (2002) Electromagnetic induction in the oceans and the anomalous behaviour of coastal C-responses for periods up to 20 days. Geophys Res Lett 29(12):1595. doi:10.1029/2001GL014409

Landauer R (1952) The electrical resistance of binary metallic mixtures. J sppl Phys 23:779

Litasov KD (2011) Physicochemical conditions for melting in the Earth's mantle containing a C–O–H fluid (from experimental data). Russ Geol Geophys 52. doi:10.1016/j.rgg.2011.04.001

Litasov KD, Ohtani E (2002) Phase relations and melt compositions in CMAS-pyrolite-H_2O system up to 25 GPa. Phys Earth Planet Int 134:105
Litasov KD, Ohtani E (2003) Stability of various hydrous phases in CMAS pyrolite-H_2O system up to 25 GPa. Phys Chem Miner 30:147
Litasov KD, Ohtani E (2007) Effect of water on the phase relations in Earths mantle and deep water cycle. In: Ohtani E (ed) Advances in high-pressure mineralogy, Geol Soc Amer Spec Pap, vol 421, p 115
Litasov KD, Ohtani E (2009) Solidus and phase relations of carbonated peridotite in the system CaO–Al_2O_3–MgO–SiO_2–Na_2O–CO_2 to the lower mantle depths. Phys Earth Planet Inter 177:46
Litasov KD, Ohtani E, Sano A (2006) Influence of water on major phase transitions in the Earths mantle. In: Jacobsen SD, van der Lee S (eds) Earths deep water cycle, geophysical monograph series, vol 168. American Geophysical Union, p 95111
Litasov KD, Ohtani E, Kagi H, Jacobsen SD (2007) Temperature dependence and mechanism of hydrogen incorporation in olivine at 12.5-14 GPa. Geophys Res Lett 34:L16314. doi:10.1029/2007GL030737
Litasov KD, Shatskiy A, Ohtani E, Katsura T (2011) Systematic study of hydrogen incorporation into Fe-free wadsleyite. Phys Chem Miner 38:75
Lu R, Keppler H (1997) Water solubility in pyrope to 100kbar. Contrib Mineral Petrol 129:35
Manthilake M, Matsuzaki T, Yoshino T, Yamashita S, Ito E, Katsura T (2009) Electrical conductivity of wadsleyite as a function of temperature and water content. Phys Earth Planet Int. doi:10.1016/j.pepi.2008.06.001
Maumus J, Bagdassarov N, Schmeling H (2005) Electrical conductivity and partial melting of mafic rocks under pressure. Geochim Cosmochim Acta 69:4703. doi:10.1016/j.gca.2005.05.010
McCammon C (2005) The paradox of mantle redox. Science 308:807
Metropolis N, Rosenbluth AW, Rosenbluth MN, Teller AH, Teller E (1953) Equation of state calculations by fast computing machines. J Chem Phys 21:1087
Mierdel K, Keppler H, Smyth JR, Langenhorst F (2007) Water solubility in aluminous orthopyroxene and the origin of Earth's asthenosphere. Science 315:364
Mosenfelder JL, Deligne LI, Asimow PD, Rossman GR (2006) Hydrogen incorporation in olivine from 2–12 GPa. Am Min 91:285
Mookherjee M, Karato S-I (2010) Solubility of water in pyrope-rich garnet at high pressures and temperature. Geophys Res Lett 37. doi:10.1029/2009GL041289
Mosegaard K, Tarantola A (1995) Monte Carlo sampling of solutions to inverse problems. J Geophys Res 100:12431. doi:10.1029/94JB03097
Nakagawa T, Tackley PJ, Deschamps F, Connolly JAD (2009) Incorporating self-consistently calculated mineral physics into thermochemical mantle convection simulations in a 3-D spherical shell and its influence on seismic anomalies in Earth's mantle. Geochem Geophys Geosyst 10:Q03004. doi:10.1029/2008GC002280
Ni H, Keppler H, Behrens H (2011) Electrical conductivity of hydrous basaltic melts: implications for partial melting in the upper mantle. Contrib Mineral Petrol. doi:10.1007/s00410-011-0617-4
Novella D, Frost DJ, Hauri EH, Bureau H, Raepsaet C, Roberge M (2014) The distribution of H_2O between silicate melt and nominally anhydrous peridotite and the onset of hydrous melting in the deep upper mantle. Earth Planet Sci Lett 400:1
Nover G (2005) Electrical properties of crustal and mantle rocks—a review of laboratory measurements and their explanation. Surv Geophys 26:593. doi:10.1007/s10712-005-1759-6
O'Neill HStC, Rubie DC, Canil D, Geiger CA, Ross CR II, Seifert E, Woodland AB (1993) Ferric iron in the upper mantle and in transition zone assemblages: implications for relative oxygen fugacities in the mantle. In: Takahashi T, Jeanloz R, Rubie DC (eds) Evolution of the earth and planets. American Geophysical Union, Washington, DC, pp 73–88
Olsen N (1998) The electrical conductivity of the mantle beneath Europe derived from C-responses from 3 to 720 hr. Geophys J Int 133:298
Olsen N (1999) Longperiod (30 days-1 year) electromagnetic sounding and the electrical conductivity of the lower mantle beneath Europe. Geophys J Int 138:179
Omura K, Kurita K, Kumazawa M (1989) Experimental study of pressure dependence of electrical conductivity of olivine at high temperatures. Phys Earth Planet Int 57:291
Park SK, Ducea MN (2003) Can in situ measurements of mantle electrical conductivity be used to infer properties of partial melts? J Geophys Res 108:2270. doi:10.1029/2002JB001899
Partzsch GM, Schilling FR, Arndt J (2000) The influence of partial melting on the electrical behaviour of crustal rocks: laboratory examinations. Model calculations and geological interpretations. Tectonophysics 317:189

Pearson DG, Brenker FE, Nestola F, McNeill J, Nasdala L, Hutchinson MT, Marveev S, Mather K, Silversmit G, Schmitz S, Vekemans B, Vincze L (2014) Hydrous mantle transition zone indicated by ringwoodite included within diamond. Nature 507:221. doi:10.1038/nature13080
Peslier AH (2010) A review of water contents of nominally anhydrous natural minerals in the mantles of Earth, Mars and the Moon. J Volcanol Geotherm Res 197:239
Peslier AH, Woodland AB, Bell DR, Lazarov M (2010) Olivine water contents in the continental lithosphere and the longevity of cratons. Nature 467:78. doi:10.1038/nature09317
Peslier AH, Bizmis M (2015) Water in Hawaiian peridotite minerals: a case for a dry metasomatized oceanic mantle lithosphere. Geochem Geophys Geosyst 16. doi:10.1002/2015GC005780
Piazzoni AS, Steinle-Neumann G, Bunge HP, Dolejs D (2007) A mineralogical model for density and elasticity of the Earths mantle. Geochem Geophys Geosyst 8:Q11010. doi:10.1029/2007GC001697
Poli S, Schmidt MW (2002) Petrology of subducted slabs. Ann Rev Earth Planet Sci 30:207
Poe B, Romano C, Nestola F, Smyth JR (2010) Electrical conductivity anisotropy of dry and hydrous olivine at 8 GPa. Phys Earth Planet Inter 181:103
Pommier A (2014) Interpretation of magnetotelluric results using laboratory measurements. Surv Geophys 35:41. doi:10.1007/s10712-013-9226-2
Pommier A, Le Trong E (2011) "SIGMELTS": a web portal for electrical conductivity calculations in geosciences. Comput Geosci 37. doi:10.1016/j.cageo.2011.01.002
Pommier A, Gaillard F, Malki M, Pichavant M (2010) Reevaluation of the electrical conductivity of silicate melts. Am Mineralog 95:284
Püthe C, Kuvshinov A, Khan A, Olsen N (2015) A new model of Earth's radial conductivity structure derived from over 10 years of satellite and observatory magnetic data. Geophys J Int 203(3):1864–1872. doi:10.1093/gji/ggv407
Rauch M, Keppler H (2002) Water solubility in orthopyroxene. Contrib Mineralog Petrol 78:99
Ricard Y, Mattern E, Matas J (2005) Synthetic tomographic images of slabs from mineral physics. In: van der Hilst RD (ed) Earths deep mantle: structure, composition, and evolution, geophys. monogr. ser., vol 160. AGU, Washington, DC, , pp 283–300
Ringwood A (1975) Composition and structure of the earth's mantle. McGraw-Hill, New York
Ritsema J, Xu W, Stixrude L, Lithgow-Bertelloni C (2009) Estimates of the transition zone temperature in a mechanically mixed upper mantle. Earth Planet Sci Lett 244. doi:10.1016/j.epsl.2008.10.024
Ritsema J, van Heijst HJ, Deuss A, Woodhouse JH (2011) S40RTS: a degree-40 shear velocity model for the mantle from new Rayleigh wave dispersion, teleseismic travel times, and normal-mode splitting function measurements. Geophys J Int 184:1223. doi:10.1111/j.1365-246X.2010.04884.x
Roberts JJ, Tyburczy JA (1993) Impedance spectroscopy of single and polycrystalline olivine: evidence for grain boundary transport. Phys Chem Miner 20:19
Roberts JJ, Tyburczy JA (1999) Partial-melt electrical conductivity: influence of melt composition. J Geophys Res 104:7055
Romano C, Poe BT, Kreidie N, McCammon CA (2006) Electrical conductivities of pyrope-almandine garnets up to 19 GPa and 1700 °C. Am Mineral 91:1371
Romano C, Poe BT, Tyburczy J, Nestola F (2009) Electrical conductivity of hydrous wadsleyite. Eur J Mineral 21:615622
Rohrbach A, Ballhaus C, Golla-Schindler U, Ulmer P, Kamenetsky VS, Kuzmin DV (2007) Metal saturation in the upper mantle. Nature 449:456
Sakurai M, Tsujino N, Sakuma H, Kawamura K, Takahashi E (2014) Effects of Al content on water partitioning between orthopyroxene and olivine: implications for lithosphere-asthenosphere. Earth Planet Sci Lett 400:284. doi:10.1016/j.epsl.2014.05.041
Samrock F, Kuvshinov A (2013) Tippers at island observatories: can we use them to probe electrical conductivity of the Earth's crust and upper mantle? Geophys Res Lett 40:824
Schaeffer AJ, Lebedev S (2013) Global shear-speed structure of the upper mantle and transition zone. Geophys J Int 194:417–449
Schock RN, Duba AG, Shankland TJ (1989) Electrical conduction in olivine. J Geophys Res 94:5829
Schultz A, Kurtz RD, Chave AD, Jones AG (1993) Conductivity discontinuities in the upper mantle beneath a stable craton. Geophys Res Lett 20:2941. doi:10.1029/93GL02833
Seifert KF, Will G, Voigt R (1982) Electrical conductivity measurements on synthetic pyroxenes MgSiO3 FeSiO3 at high pressures and temperatures under defined thermodynamic conditions. In: Schreyer W (ed) High-pressure researches in geoscience. Stuttgart, Germany: Schweizerbart, p 41932
Shankland TJ (1975) Electrical conduction in rocks and minerals: parameters for interpretation. Phys Earth Planet Int 10:209
Shankland TJ (1979) Physical properties of minerals and melts. Rev Geophys Space Phys 17:792

Shankland TJ, Waff HS (1977) Partial melting and electrical conductivity anomalies in the upper mantle. J Geophys Res 82:54095417
Shankland TJ, Ander ME (1983) Electrical conductivity, temperature, and fluids in the lower crust. J Geophys Res 88:9475
Shankland TJ, Duba A (1990) Standard electrical conductivity of isotropic, homogeneous olivine in the temperature range 1200–1500 °C. Geophys J Int 103:25
Shankland TJ, O'Connell RJ, Waff HS (1981) Geophysical constraints on partial melt in the upper mantle. Rev Geophys Space Phys 19:394
Shapiro NM, Ritzwoller MH (2004) Thermodynamic constraints on seismic inversions. Geophys J Int 157:1175. doi:10.1111/j.1365-246X.2004.02254.x
Simpson F (2001) Resistance to mantle flow inferred from the electromagnetic strike of the Australian upper mantle. Nature 412:632–635
Smyth JR (1987) β-Mg_2SiO_4 a potential host for water in the mantle? Am Mineralog 72:1051
Smyth JR, Frost DJ (2002) The effect of water on the 410-km discontinuity: an experimental study. Geophys Res Lett 29:1485. doi:10.1029/2001GL014418
Smyth JR, Jacobsen SD (2006) Nominally anhydrous minerals and Earth's deep water cycle. In: van der Lee S, Jacobsen SD (eds) Earth's deep water cycle. American Geophysical Union Monograph Series, vol 168, p 1
Sobolev SV, Babeyko A (1994) Modeling of mineralogical composition, density and elastic wave velocities in anhydrous magmatic rocks. Surv Geophys 15:515
Stixrude L, Lithgow-Bertelloni C (2005) Mineralogy and elasticity of the oceanic upper mantle: origin of the low-velocity zone. J Geophys Res 110:B03204. doi:10.1029/2004JB002965
Stixrude L, Lithgow-Bertelloni C (2011) Thermodynamics of mantle minerals II. Phase equilibria. Geophys J Int 184:1180. doi:10.1111/j.1365-246X.2010.04890.x
Tackley PJ (2000) Mantle convection and plate tectonics: towards an integrated physical and chemical theory. Science 288:2002
Tackley PJ (2012) Dynamics and evolution of the deep mantle resulting from thermal, chemical, phase and melting effects. Earth Sci Rev 110:1. doi:10.1016/j.earscirev.2011.10.001
Tackley PJ, Xie S, Nakagawa T, Hernlund JW (2005) Numerical and laboratory studies of mantle convection: philosophy, accomplishments and thermo-chemical structure and evolution. In: Earth's deep mantle: structure, composition, and evolution, geophysical monograph series vol 160, p 83. AGU. doi:10.1029/160GM07
Tarantola A, Valette B (1982) Inverse problems = quest for information. J Geophys 50:159
ten Grotenhuis SM, Drury MR, Peach CJ, Spiers CJ (2004) Electrical properties of fine-grained olivine: evidence for grain boundary transport. J Geophys Res 109:B06203. doi:10.1029/2003JB002799
ten Grotenhuis SM, Drury MR, Spiers CJ, Peach CJ (2005) Melt distribution in olivine rocks based on electrical conductivity measurement. J Geophys Res 110:B12201. doi:10.1029/2004JB003462
Tenner TJ, Hirschmann MM, Withers AC, Hervig RL (2009) Hydrogen partitioning between nominally anhydrous upper mantle minerals and melt between 3 and 5 GPa and applications to hydrous peridotite partial melting. Chem Geol 262:42
Tenner TJ, Hirschmann MM, Withers AC, Ardia P (2012) H_2O storage capacity of olivine and low-Ca pyroxene from 10 to 13 GPa: consequences for dehydration melting above the transition zone. Contrib Mineral Petrol 163:297
Toffelmier DA, Tyburczy JA (2007) Electromagnetic detection of a 410-km-deep melt layer in the southwestern United States. Nature 441. doi:10.1038/nature05922
Tyburczy JA (2007) Properties of rocks and minerals the electrical conductivity of rocks, minerals and the Earth. Treatise Geophys 2:631
Tyburczy JA, Waff HS (1983) Electrical conductivity of molten basalt and andesite to 25 kilobars pressure: geophysical significance and implications for charge transport and melt structure. J Geophys Res 88:2413
Tyburczy JA, Fisler DK (1995) Electrical properties of minerals and melts. Mineral physics and crystallography: a handbook of physical constants. AGU Ref Shelf 2:185
Utada H, Koyama T, Shimizu H, Chave AD (2003) A semi-global reference model for electrical conductivity in the mid-mantle beneath the North Pacific region. Geophys Res Lett 30:1194. doi:10.1029/2002GL016092
Utada H, Koyama T, Obayashi M, Fukao Y (2009) A joint interpretation of electromagnetic and seismic tomography models suggests the mantle transition zone below Europe is dry. Earth Planet Sci Lett 281:249
Vacher P, Verhoeven O (2007) Modelling the electrical conductivity of iron-rich minerals for planetary applications. Planet Space Sci 55:455. doi:10.1016/j.pss.2006.10.003

Velimský J (2010) Electrical conductivity in the lower mantle: constraints from CHAMP satellite data by time domain EM induction modelling. Phys Earth Planet Inter 180:111. doi:10.1016/j.pepi.2010.02.007

Verhoeven O, Mocquet A, Vacher P, Rivoldini A, Menvielle M, Arrial PA, Choblet G, Tarits P, Dehant V, Van Hoolst T (2009) Constraints on thermal state and composition of the earths lower mantle from electromagnetic impedances and seismic data. J Geophys Res 114:B03302. doi:10.1029/2008JB005678

Waff HS (1974) Theoretical considerations of electrical conductivity in a partially molten mantle and implications for geothermobarometry. J Geophys Res 79:4003

Wannamaker PE, Caldwell TG, Jiracek GR, Maris V, Hill GJ, Ogawa Y, Bibby HM, Bennie SL, Heise W (2009) Fluid and deformation regime of an advancing subduction system at Marlborough New Zealand. Nature 460:733736

Watson HC, Roberts JJ, Tyburczy JA (2010) The effect of conductive grain boundary impurities on electrical conductivity in polycrystalline olivine. Geophys Res Lett 37:L02303. doi:10.1029/2009GL041566

Watt JP, Davies GF, O'Connell RJ (1976) The elastic properties of composite materials. Rev Geophys Space Phys 14:541

Weidelt P (1972) The inverse problem of geomagnetic induction. Z Geophys 38:257

Williams Q, Hemley RJ (2001) Hydrogen in the deep Earth. Ann Rev Earth Planet Sci 29:365

Withers AC, Hirschmann MM (2007) H_2O storage capacity of $MgSiO_3$ clinoenstatite at 8–13GPa, 1100 − 1400 °C. Contrib Mineral Petrol 154:663

Withers AC, Wood BJ, Carroll MR (1998) The OH content of pyrope at high pressure. Chem Geol 149:161

Wood BJ (1995) The effect of H_2O on the 410-kilometer seismic discontinuity. Science 268:74

Worzewski T, Jegen M, Kopp H, Brasse H, Castillo WT (2011) Magnetotelluric image of the fluid cycle in the Costa Rican subduction zone. Nat Geosci 4:108. doi:10.1038/NGEO1041

Wu X, Zhanga B, Xua J, Katsura T, Zhaid S, Yoshino T, Manthilake G, Shatskiy A (2010) Electrical conductivity measurements of periclase under high pressure and high temperature. Physica B 405. doi:10.1016/j.physb.2009.08.036

Xie S, Tackley PJ (2004) Evolution of helium and argon isotopes in a convecting mantle. Phys Earth Planet Inter 146:417. doi:10.1016/j.pepi.2004.04.003

Xu Y, Shankland TJ (1999) Electrical conductivity of orthopyroxene and its high pressure phases. Geophys Res Lett 26:2645

Xu Y, McCammon C, Poe BT (1998) The effect of alumina on the electrical conductivity of silicate perovskite. Science 282:922

Xu Y, Shankland TJ, Poe BT (2000) Laboratory-based electrical conductivity in the Earth's mantle. J Geophys Res 108:2314

Xu W, Lithgow-Bertelloni C, Stixrude L, Ritsema J (2008) The effect of bulk composition and temperature on mantle seismic structure. Earth Planet Sci Lett 275:70. doi:10.1016/j.epsl.2008.08.012

Yang X (2011) Origin of high electrical conductivity in the lower continental crust: a review. Surv Geophys 32:875

Yang X, Heidelbach F (2012) Grain size effect on the electrical conductivity of clinopyroxene. Contrib Mineral Petrol 163:939

Yoshino T (2010) Laboratory electrical conductivity measurement of mantle minerals. Surv Geophys 31:163. doi:10.1007/s10712-009-9084-0

Yoshino T, Katsura T(2009a) Reply to comments on Electrical conductivity of wadsleyite as a function of temperature and water content by Manthilake et al. Phys Earth Planet Inter. doi:10.1016/j.pepi.2009.01.012

Yoshino T, Katsura T (2009b) Effect of iron content on electrical conductivity of ringwoodite, with implications for electrical structure in the transition zone. Phys Earth Planet Int. doi:10.1016/j.pepi.2008.09.015

Yoshino T, Katsura T (2012a) Re-evaluation of electrical conductivity of anhydrous and hydrous wadsleyite. Earth Planet Sci Lett 337–338:56. doi:10.1016/j.epsl.2012.05.023

Yoshino T, Katsura T (2012b) Corrigendum. Earth Planet Sci Lett 357–358:422. doi:10.1016/j.epsl.2012.10.020

Yoshino T, Katsura T (2013) Electrical conductivity of mantle minerals: role of water in conductivity anomalies. Ann Rev Earth Planet Sci 41:605. doi:10.1146/annurev-earth-050212-124022

Yoshino T, Takuya M, Yamashita S, Katsura T (2006) Hydrous olivine unable to account for conductivity anomaly at the top of the asthenosphere. Nature 443:973

Yoshino T, Manthilake G, Matsuzaki T, Katsura T (2008a) Dry mantle transition zone inferred from the conductivity of wadsleyite and ringwoodite. Nature 451. doi:10.1038/nautre06427

Yoshino T, Nishi M, Matsuzaki T, Yamazaki D, Katsura T (2008b) Electrical conductivity of majorite garnet and its implications for electrical structure in the mantle transition zone. Phys Earth Planet Int. doi:10.1016/j.pepi.2008.04.009

Yoshino T, Matsuzaki T, Shatskiy A, Katsura T (2009) The effect of water on the electrical conductivity of olivine aggregates and its implications for the electrical structure of the upper mantle. Earth Planet Sci Lett. doi:10.1016/j.epsl.2009.09.032

Yoshino T, Laumonier M, McIsaac E, Katsura T (2010) Electrical conductivity of basaltic and carbonatite melt-bearing peridotites at high pressures: implications for melt distribution and melt fraction in the upper mantle. Earth Planet Sci Lett 295:593

Yoshino T, Ito E, Katsura T, Yamazaki D, Shan S, Guo X, Nishi M, Higo Y, Funakoshi K-I (2011) Effect of iron content on electrical conductivity of ferropericlase with implications for the spin transition pressure. J Geophys Res 116:B04202. doi:10.1029/2010JB007801

Yoshino T, McIsaac E, Laumonier M, Katsura T (2012a) Electrical conductivity of partial molten carbonate peridotite. Phys Earth Planet Int 194195. doi:10.1016/j.pepi.2012.01.005

Yoshino T, Shimojuku A, Shan S, Guo X, Yamazaki D, Ito E, Higo Y, Funakoshi K (2012b) Effect of temperature, pressure and iron content on the electrical conductivity of olivine and its high-pressure polymorphs. J Geophys Res 117:B08205. doi:10.1029/2011JB008774

Yoshino T, Shimojoku A, Li D (2014) Electrical conductivity of stishovite as a function of water content. Phys Earth Planet Int 227:48. doi:10.1016/j.pepi.2013.12.003

Young TE, Green HW, Hofmeister AM, Walker D (1993) Infrared spectroscopic investigation of hydroxyl in—$(Mg,Fe)_2$ SiO_4 and coexisting olivine: implications for mantle evolution and dynamics. Phys Chem Miner 19:409

Zhang B, Yoshino T, Wu X, Matsuzaki T, Shan S, Katsura T (2012) Electrical conductivity of enstatite as a function of water content: Implications for the electrical structure in the upper mantle. Earth Planet Sci Lett 357–358:11. doi:10.1016/j.epsl.2012.09.020

Zunino A, Connolly JAD, Khan A (2011) Precalculated phase equilibrium models for geophysical properties of the crust and mantle as a function of composition. Geochem Geophys Geosys 12:Q04001. doi:10.1029/2010GC003304